This is the peer-reviewed, final accepted version for American Mineralogist, published by the Mineralogical Society of America.
The published version is subject to change. Cite as Authors (Year) Title. American Mineralogist, in press.
DOI: https://doi.org/10.2138/am-2022-8200. http://www.minsocam.org/

Revision 2

Tin isotopes as geochemical tracers of ore-forming processes with Sn mineralization

Zhen-Hua Zhou[a*], Jing-Wen Mao[a], Jia-Qi Zhao[a], Xu Gao[a, b], Stefan Weyer[b], Ingo Horn[b], Francois Holtz[b], Paolo A. Sossi[c], Da-Chuan Wang[b]

[a] *MNR Key Laboratory of Metallogeny and Mineral Assessment, Institute of Mineral Resources, CAGS, Beijing 100037, China*

[b] *Institut für Mineralogie, Leibniz Universität Hannover, Callinstr. 3, 30167 Hannover, Germany*

[c] *Institute of Geochemistry and Petrology, ETH Zürich, Sonneggstrasse 5, CH-8092 Zürich, Switzerland*

Abstract

[*] Corresponding author.
E-mail address: zhzhoucags@sina.com (Zhenhua Zhou)

Tin is a key strategic metal and indispensable in the high-tech industry. Constraining the source of the mineralizing fluids, their pathways and subsequent ore-forming process are fundamental to optimizing tin exploration and efficient mining operations. Here, we present trace element analysis, LA-ICPMS mapping, and the first systematic high-precision *in situ* Sn isotope analysis of cassiterite from several tin deposits (i.e., Weilasituo, Baiyinchagan, Maodeng Sn-polymetallic deposits) in northeast China using UV-*f*s-LA-ICPMS. We show that the distribution of trace elements in cassiterite from these localities reflects crystallization under disequilibrium conditions with coexisting fluids or melts, and suggests intense fluid-rock reactions. Among the three deposits, cassiterite from the Maodeng Sn-Cu deposit has the heaviest weighted mean Sn isotope composition, with $\delta^{124}/^{117}$Sn values ranging from 0.11 ± 0.04 ‰ to 0.62 ± 0.08 ‰. The Baiyinchagan Sn-Ag-Pb-Zn deposit displays the lightest isotope composition with $\delta^{124}/^{117}$Sn values ranging from -1.43 ± 0.06 ‰ to -0.50 ± 0.04 ‰. While, the Weilasituo Sn-W-Li-polymetallic deposit shows the largest spread in $\delta^{124}/^{117}$Sn values, ranging from -0.66 ± 0.05 ‰ to 0.59 ± 0.03 ‰. The Sn isotope variability in these natural cassiterites is attributed to Sn isotope fractionation associated with the diversity of Sn mineralization pathways and different physicochemical conditions. Furthermore, the $\delta^{124}/^{117}$Sn values of cassiterite from the Maodeng and Baiyinchagan deposits gradually decrease from early to late mineralization stages, suggesting they were generated by Rayleigh fractionation during progressive mineral precipitation from a hydrothermal fluid. In contrast, heavy Sn isotope values in late-stage Weilasituo cassiterites are likely a result of disequilibrium fluid-rock interaction with external, wall rock-derived fluids. Our results reveal that liquid-vapor partitioning or fluid-rock interaction may have more influence on Sn isotope fractionation between cassiterite and evolving ore-forming fluids than does magmatic differentiation, pH, pressure and temperature during formation of tin deposits. According to the tin isotopic data obtained so far from this study and published previously, we observe no relationship between the Sn isotope composition of cassiterite and the age of mineralization or tectonic setting. However, cassiterite displays heavier Sn isotope compositions than coexisting stannite (Cu_2FeSnS_4) regardless of the deposit type and depth of emplacement, suggesting that redox state may influence Sn isotope fractionation. More importantly, we first recognize a general shift towards light Sn isotope compositions in cassiterite associated with

decreasing Ti/Zr ratios, suggesting that Sn isotopes can be a robust tool identifying the source of the mineralization. Furthermore, based on our Sn isotope data together with previous studies of fluid inclusion, we propose that the dominant Sn (II) species occur in early ore mineralization systems, then shifts to the Sn (IV) species in late stage due to redox change or higher Cl^- activity. Tin isotopes may be a robust tool to trace the mineralization center and fluid pathways, and to ascertain the mechanisms of metal precipitation.

Key words: Fluid-rock interaction; Liquid-vapor partitioning; Kinetic Rayleigh fractionation; *In situ* Sn isotope; Sn deposits

1. INTRODUCTION

Tin has ten stable isotopes that have the largest mass range (i.e., mass 112 to 124) of any element in the periodic table (Mcnaughton and Rosman, 1991; Clayton et al., 2002). Moreover, Sn is a volatile as well as chalcophile and siderophile element in terms of geochemical behavior, which makes it possible to use Sn isotopes to trace processes associated with the formation of ore mineralization, as well their interaction between fluids and vapors (Creech et al., 2017). The so-called "non-traditional" stable isotopes (e.g., Fe, Cu, Zn, Sn, W, etc.) have enjoyed increasingly commonplace usage in studies of the high-temperature geochemical evolution of magmatic-hydrothermal systems thanks to the development of modern multi-collector inductively coupled plasma mass spectrometers (MC-ICPMS) (e.g., Graham et al., 2004; Weyer and Ionov, 2007; Teng et al., 2008; Mathur et al., 2009, 2017; Dauphas et al., 2014; Wawryk and Foden, 2015; Günther et al., 2017; Sossi et al., 2018; Liu et al., 2019). Specifically, these isotope systems provide new insights on the source of metals and ore-forming processes in magmatic-hydrothermal systems. However, although the composition of Sn isotopes have been measured in numerous studies on geological, meteoritic and archaeological samples (e.g., De Laeter et al., 1965, 1967; Mcnaughton and Rosman, 1991; Haustein et al., 2010; Yamazaki et al., 2014; Mason et al., 2020; Creech et al., 2017, 2019a, b; Mathur et al., 2017) and experimental studies (Hu et al.,

1999; Polyakov et al., 2005; Dauphas et al., 2017; Wang et al., 2019; Roskosz et al., 2020; She et al., 2020), there have been relatively few studies focusing on the effect of igneous processes on Sn isotope fractionation (Badullovich et al., 2017; Wang et al., 2017, 2018). In particular, the applicability of Sn isotopes for tracing the formation of ore deposits is not yet well understood (Clayton et al., 2002; Yamazaki et al., 2013; Brügmann et al., 2017; Yao et al., 2018; Wang et al., 2019). Existing studies proposed that Sn isotope fractionation may take place during geological processes such as magmatic fractionation in the course of partial melting or fractional crystallization processes (Creech et al., 2017; Badullovich et al., 2017; Wang et al., 2018), redox reactions (Yao et al., 2018; Wang et al., 2019) and liquid-vapor partitioning (Wang et al., 2019; She et al., 2020; Wang et al., 2021), but it remains unclear which mechanisms are most significant in nature. Furthermore, all previous Sn isotope analyses were performed on solutions after digestion and purification of bulk samples. Owing to the volatile nature of Sn, isotope fractionation during sample preparation (e.g., reduction of cassiterite and purification processes) is a constant concern (Schulze et al., 2017). Isotope analysis with using femtosecond laser sampling (fs-LA-MC-ICPMS) enables time-saving, spatially resolved, precise and accurate Sn isotopes measurement. Compared to bulk analysis, this method uses far less sample and avoids the potential isotope fractionation effects associated with sample dissolution and purification.

Understanding the origins of tin deposits is of great significance for ore prospecting and their efficient exploitation. Cassiterite (SnO_2) and stannite (Cu_2FeSnS_4) are the two main carriers of Sn in tin deposits. These deposits are mostly related to granitic suites, and in particular reduced, peraluminous S-type granites from which magmatic-hydrothermal fluids are derived (Černý et al., 2005; Lehmann, 2020). Consequently, the Sn isotope composition and distribution of trace elements in cassiterite could be key geochemical tracers of the evolution of Sn-bearing magmatic-hydrothermal ore systems (Möller et al., 1988; Murciego et al., 1997; Brügmann et al., 2017; Cheng et al., 2019; Yao et al., 2018; Mao et al., 2020). However, the systematics of Sn isotope fractionation between fluid and cassiterite must first be established before they can be applied as indicators for the genesis of a particular Sn-bearing ore deposit. In this contribution, the trace element and Sn isotope compositions, including the first high-precision *in situ* Sn isotope ratio measurements, of cassiterite from

various tin deposits in the Southern Great Xing'an Range (SGXR), NE China were obtained by LA-ICPMS and UV-*fs*-MC-ICPMS. These deposits include magmatic-hydrothermal vein type (e.g., Weilasituo Sn-polymetallic deposit), hydrothermal-vein type (e.g., Baiyinchagan Sn-Ag-Pb-Zn deposit), and cassiterite-sulfide type (e.g., Maodeng Sn-Cu deposit) tin mineralizations, which are all related to granitic magma with distinct degrees of differentiation, melt compositions and temperature of mineralization. Our aim is to test the potential of using Sn isotopes to monitor the mineralization environment and ore-forming processes, and to further improve our understanding of the mechanisms resulting in Sn isotopic fractionation in magmatic-hydrothermal systems.

2. GEOLOGICAL SETTING AND THE STUDIED SAMPLES

The SGXR is located in the eastern Inner Mongolia, northeast China, which is bordered by several major fault- and suture zones (Fig. 1a, b). The SGXR comprises a segment of the southeastern edge of the Central Asian orogenic belt. The Precambrian basement rocks in the SGXR constitute a khondalitic sequence of sillimanite- and garnet-bearing gneisses, hornblende-plagioclase gneisses and felsic ortho- and paragneisses (Zhou et al., 2011). The early Paleozoic medium- to high-grade metamorphic complex of the Xilinhot massif constitutes the oldest formation in this area (Shi et al., 2003). The Ordovician to Carboniferous strata are composed mainly of detrital metasedimentary units, carbonate rocks, and volcanic rocks (Wang et al., 2001). Permian mafic to intermediate-felsic volcanic rocks are well developed and constitute the ore-hosting rocks for most Sn deposits in the region (Wang et al., 2001). Mesozoic volcanic-sedimentary sequences are the major cover in this area, consisting of intermediate-felsic volcanic rocks. Granitoids are widely distributed in the area, which mostly of Mesozoic granitic-granodioritic intrusive rocks. The triangular tectonic framework is delineated by the principal sets of NE-NNE and NW faults, as well as E-W basement faults.

In the Mesozoic, various composite folds today defined by the Huanggang-Ganzhu'ermiao anticline also formed, which control the distribution characteristics of ore-forming rocks and ore deposits. The SGXR is an important Sn and base metal province, evidenced by the multitude of Sn deposits that have been discovered there

(Fig. 1b). The ages of mineralization associated with ore-forming events are mainly in the range of 149 to 133 Ma, while the related granitoids have ages between 150 and 135 Ma (Mao et al., 2019 and references herein). The cassiterite- and sulfide-bearing veins are the most abundant ore type in the SGXR, although there are minor skarn, greisen, and porphyry Sn ore occurrences.

The large-scale Sn deposit in the Weilasituo granite stock (a reserve of 89,800 t Sn metal and averaging 0.80% Sn) exhibits concentric zoning in its mineralizing assemblage about the granitic source rocks: disseminated Nb-Ta-Sn mineralization can be found in the granite itself, while its rim is composed of a Sn-rich greisen and Sn-rich quartz veins, with yet more distal mineralization dominated by Ag-Pb-Zn-rich veins (Gao et al., 2019). The vein mineralization is mainly hosted in the biotite plagioclase gneiss of the Xilinguole Formation (Fig. 1c), and the ore-related quartz porphyry is a highly differentiated I-type granite characterized by remarkable REE tetrad effect (TE_{1-3}) (Supplemental Table 1). Two episodes of mineralizing events have been identified with ages of 135–138 Ma and 122–130 Ma, respectively (Supplemental Table 1) (Wang et al., 2017; Liu et al., 2018a; Gao et al., 2019). Four main ore-forming stages are identified in the Weilasituo deposit, i.e., a magmatic stage, a magmatic-hydrothermal transition stage, a high-temperature hydrothermal stage, and a late hydrothermal stage (Gao et al., 2019). The ore-forming fluid was characterized by high Na and F concentrations, indicative of a magmatic origin (Wang et al., 2017). The main stage (high–temperature hydrothermal stage) of the mineralization likely occurred in a temperature range of 243 to 473 °C, according to the microthermometry results of fluid inclusions. Moreover, Liu et al. (2018b) proposed that significant boiling or immiscibility occurred in the mineralization process, based on detailed fluid inclusions studies.

The Baiyinchagan Sn-Ag-Pb-Zn (Sb) deposit is the largest Sn mineralization in the SGXR, with a reserve of 223,400 t Sn metal and averaging 0.76% Sn (Yao et al., 2017). It is located in the westernmost SGXR (Fig. 1b). The tin mineralization occurs mainly as cassiterite-quartz-sulfide veins and as cassiterite in breccias, hosted by both Cretaceous quartz porphyry and lower Permian tuffaceous siltstone (Fig. 1d). Additionally, tin ores form cassiterite-quartz-chlorite-bearing veins are also hosted by several large fault fracture zones at depth in the lode. Yao et al. (2017) obtained U-Pb zircon ages of 141.7 ± 0.8 to 140.2 ± 1.1

Ma for the quartz porphyry, which are consistent with the cassiterite U-Pb age of 140.0 ± 12 Ma (MSWD=5.8). The differentiation degree of Baiyinchagan ore-related rocks is lower than that of Weilasituo (Fig. 2), while the granite crystallization temperature overlaps with, but is marginally higher in Baiyinchagan than that in Weilasituo (Supplemental Table 1). Four main mineralization stages are recognized, namely a late magmatic stage, a cassiterite-quartz stage, a cassiterite-sulfide stage, and a low temperature hydrothermal stage. The chemical nature of the ore-forming fluids have not yet been studied, but the mineralization temperature (cassiterite-sulfide stage and low temperature hydrothermal stage) calculated from the sphalerite thermometer (e.g., Keith et al., 2014) was 265–381 ℃ (Liu et al., 2017).

The Maodeng mine exploits a high grade, lode-type Sn-Cu deposit in the SGXR, with a reserve of 5,817 t Sn metal and averaging 1.26% Sn. Both tin and copper mineralization are associated with strong chloritic alteration, which is superimposed on an earlier episode of sericitization and tourmaline-quartz veining. The tin and copper ores show three stages of vein growth: quartz-cassiterite (-wolframite), base-metal sulfides, and late veinlets and crusts (quartz-calcite-fluorite veins). These are hosted by both Cretaceous porphyritic granite and lower Permian carbonaceous metamorphosed siltstone (Fig. 1e). The porphyritic granites possess a high oxygen fugacity on the basis of high Fe^{3+}/Fe^{2+} ratios (Fig. 2a) and a relatively high crystallization temperature (867–892℃) relative to the other Sn-bearing granites (Supplemental Table 1). These features reflect its lower degree of differentiation (~ 70 wt. % SiO_2) compared to the Weilasituo (~73 wt. %) and Baiyinchagan (~76 wt. %) granites. The porphyritic granite has a U-Pb zircon age of 132.1 ± 0.7 Ma and cassiterite U-Pb age of 140 ± 20 Ma (Guo et al., 2019). Fluid inclusion studies indicate that the ore-forming fluid is predominantly composed of H_2O-NaCl±CO_2±H_2±CH_4, and is moderately saline (8–15 % NaCleqv.) with a highly variable temperature range over which mineralization occurred (220–560 ℃) (Liu, 1996).

3. SAMPLES AND ANALYTICAL METHODS

3.1. Samples and sample preparation

Twenty-three cassiterite samples from the three tin deposits (Weilasituo, Baiyinchagan, Maodeng) were selected for Sn isotope analysis. A detailed description of the quartz veins

and various mineralization stages is given in Table 1. The quartz-cassiterite-sulfide veins were crushed, hand washed, and purified under a binocular microscope to separate the cassiterite samples. The cassiterite grains were mounted in epoxy blocks and polished for further analysis. Transmitted-light images, reflected-light images, and cathodoluminescence (CL) images of the investigated cassiterites were examined in order to avoid the ablation of fluid and mineral inclusions during LA-ICPMS analyses.

3.2. Cassiterite SEM-CL imaging

Scanning electron microscopy (SEM)-CL imaging has been performed on resin targets to distinguish different cassiterite bands, which are usually not visible in hand samples or under transmitted-light microscopy. The resin target was cleaned by ultrasonication and then coated with carbon before analysis. The CL images were obtained at the Nanjing Hongchuang Geoanalysis Co., Ltd. with Tescan MIRA3 LM instrument equipped with a CL detector. The applied accelerating voltage and current were set at constant values of 7 kV and 1.2 nA, respectively. Each CL image was collect by 80 s accumulation time and shared about a 15% overlapping area with the surrounding images to ensure seamless stitching panorama.

3.3. Laser ablation-ICPMS mapping and *in situ* trace element analysis

In situ trace element mapping and analysis of cassiterite was conducted using LA-ICPMS in the State Key laboratory of ore deposit geochemistry, Institute of Geochemistry, Chinese Academy of Sciences and Nanjing Hongchuang Exploration Technology Service Co., Ltd. The ATL (ATLEX 300) excimer laser and a Two Volume S155 ablation cell were equipped in the Resolution SE model laser ablation system (Applied Spectra, USA). An Agilent 7900 ICPMS (Agilent, USA) was coupled to the laser ablation system.

Detailed tuning parameters are similar as reported in Thompson et al. (2018). LA-ICPMS tuning was performed using a 50 micron diameter line scan at 3 μm/s on NIST 612 at ~3.5 J/cm^2 with repetition rate 10 Hz, with the objective of adjusting the gas flow to obtain the highest sensitivity (^{238}U~6*10^5 cps) and the lowest oxide ratio (ThO/Th<0.2%). Once achieved, a pulse-to-analog (P/A) calibration were conducted on the NIST 610 glass

This is the peer-reviewed, final accepted version for American Mineralogist, published by the Mineralogical Society of America.
The published version is subject to change. Cite as Authors (Year) Title. American Mineralogist, in press.
DOI: https://doi.org/10.2138/am-2022-8200. http://www.minsocam.org/

using a 100 micron diameter line scan. Other laser parameters are identical to those reported in Thompson et al. (2018). For LA-ICPMS mapping, the nominal masses analyzed were ^{45}Sc, ^{47}Ti, ^{51}V, ^{55}Mn, ^{57}Fe, ^{90}Zr, ^{93}Nb, ^{118}Sn, ^{121}Sb, ^{178}Hf, ^{181}Ta, ^{182}W and ^{238}U, with a total scan time of ~ 1 second. While, for trace element analysis, the nominal masses analyzed were ^{7}Li, ^{27}Al, ^{45}Sc, ^{47}Ti, ^{52}Cr, ^{57}Fe, ^{90}Zr, ^{93}Nb, ^{118}Sn, ^{121}Sb, ^{181}Ta, ^{182}W and ^{238}U, with a total scan time of ~ 0.21 seconds. A pre-ablation step was conducted for each spot measurement using 5 laser shots (~1 μm in depth) to avoid any potential surface contamination. The LA-ICPMS mapping was performed using 20 μm diameter square line at 5 μm/s with a repetition rate 10 Hz and at a fluence of 4 J/cm^2. Individual trace element analyses were performed using 50 μm diameter spot at 10 Hz and a fluence of 6 J/cm^2.

The data was reduced using the Iolite software package (Paton et al., 2011). NIST 610 was used as the primary reference material, while BHVO-2G and BIR-1G were used as secondary reference materials. Triplicates of the reference materials were bracketed between multiple groups of 10 to 12 sample unknowns. In general, 35-40 seconds of the sample signal was attained following a 20 second gas background analysis. The ^{118}Sn was used as an internal standard for calibrating the contents of trace elements, assuming stoichiometric SnO_2 for quantification purposes.

3.4. MC-ICPMS Sn isotope measurements

All Sn isotope analyses of the cassiterite samples were performed at the Institute of Mineralogy of the Leibniz University of Hannover (Germany), using a UV femtosecond laser ablation device coupled to a Thermo Finnigan Neptune Plus multi-collector ICPMS (Horn et al., 2006; Horn and Von Blanckenburg, 2007), following the protocol and the settings described in Schulze et al. (2017). The laser system used in this study is based on a 100-femtosecond Ti-sapphire regenerative amplifier system (Spectra Physics Solstice, USA) described in detail by Horn and Von Blanckenburg (2007). Depending on the sample size, the spot diameter and recurrence rate of the beam varied from 35 to 45 μm, and from 5 to 2 Hz, respectively, yielding signal intensities from 15 to 25 V on mass ^{117}Sn. The total analysis time for each spot was about 180 s, including 30 s of background scanning (with the laser switched off). A combined standard-sample-standard bracketing and external mass bias

monitoring method (Li et al., 2009; Marechal et al., 1999) has been performed, using a Sb standard solution (*SPEX*) that was aspirated and subsequently combined with the laser ablation sample for simultaneous isotope analyses. For mass bias correction, a true isotope ratio of 0.7479 for $^{123}Sb/^{121}Sb$ (She et al., 2020; Schulze et al., 2017) was applied using the exponential fractionation law (Russell et al., 1978).

Due to the very low abundances of the low mass isotopes ^{112}Sn (0.97%), ^{114}Sn (0.65%), ^{115}Sn (0.36%) (Meija et al., 2016), only the seven high mass Sn isotopes (mass 117-120, 122, and 124) were measured using a collector configuration with Faraday detectors connected to 10^{11} ohm amplifiers, as given in Schulze et al. (2017). Correction of isobaric interferences of Te isotopes on ^{120}Sn, ^{122}Sn, ^{124}Sn and ^{123}Sb was monitored by simultaneous measurement of the interference-free ^{125}Te. Due to the interference of ^{123}Te on ^{123}Sb, which was used as a mass bias monitor, a four-step iterative procedure was used in order to perform a mass-bias corrected interference correction, assuming natural Te isotope abundances for the first iteration (see Schulze et al. (2017)).

In house standards were used because there are no certified Sn or Sb isotope standards available. A rod of pure Sn (99.9% Sn) with an isotopic composition indistinguishable from that of *SPEX* was selected as bracketing standard for the laser ablation analyses (Schulze et al., 2017). These authors also extensively tested the suitability of the tin rod as a bracketing standard for Sn isotope analyses of cassiterite. The pure Sn rod was measured in a standard-sample bracketing arrangement between every three to five samples. The Sn isotope compositions of the samples are reported as δ-values relative to the Sn rod (or equally to Sn *SPEX*). The uncertainty of individual analysis (i.e., internal precision) is given as twofold standard error of the mean (i.e., 2 SE = 2 SD/$N^{0.5}$; N, the number of cycles) of the ~ 120 1s integrations. All averages of replicate measurements are given as twofold standard deviation 2 SD (external reproducibility). The overall external reproducibility is better than 0.1 ‰ for $^{124}Sn/^{117}Sn$ relative to Sn rod (Schulze et al., 2017; Liu et al., in press).

4. RESULTS

4.1. Cassiterite CL textures and trace element mapping

Cathodoluminescence images effectively reveal the internal microtextures of cassiterite

from different tin deposits in SGXR (Fig. 3). Three generations of cassiterite from the Weilasituo deposit can be identified based on their distinctive intensity and CL zoning features (Cst I, II, and III). The CL intensity of Cst I is very low, generally appearing homogeneous and dark in CL images (Fig. 3a-d). However, oscillatory zoning marked by alternating thin bands with slightly different CL intensities can be locally identified (Fig. 3c). Most of these cassiterites are euhedral to subhedral and 200–500 μm in size. By contrast, the Cst II phases with sizes up to 300–600 μm are characterized by bright luminescence and clear oscillatory growth zonation (Fig. 3a-d). Cst II occurs as either individual crystals or as overgrowths on preexisting Cst I grains. The CL intensity of Cst III is higher than that of Cst I and Cst II, which were themselves truncated or overgrown by Cst III veinlets (Fig. 3d). The dimensions of the Cst III crystals are commonly smaller than 40 μm. Therefore, trace element analysis with a sufficient resolution could not be performed on Cst III phases.

The cassiterite grains from the Baiyinchagan and Maodeng localities are generally homogeneous and only one generation can be observed based on the representative SEM-CL images. Cassiterite from the Baiyinchagan deposit are generally anhedral (Fig. 3e), with low CL intensity, small size (100–300 μm) and no oscillatory zoning. In contrast, the Maodeng cassiterite samples are generally prismatic and bipyramidal (Fig. 3f), and show bright luminescence with clear oscillatory growth zonation. These grains are mostly 300–500 μm in size.

Trace element mapping results show a direct relationship between element distribution and the zoning defined by the CL intensities, indicating that the variations in CL signals are due to intra-grain compositional variations (e.g., Murciego et al., 1997; Cheng et al., 2019). Below, we discuss two representative samples from Weilasituo (NW-N-72) and Maodeng (WM-7) in more detail. Aluminium, Ti, W (V) are thought to promote CL intensity, producing bright luminescence of cassiterite, whereas high concentrations of Fe, (Si, Fe) and (Nb, Ta) result in low luminescence (Hall and Ribbe, 1971; Farmer et al., 1991; Wille et al., 2018). The LA-ICPMS mapping results indicate that the Weilasituo cassiterites are chemically zoned. The dark-luminescing Cst I is enriched in Fe, W, Nb, Zr, Hf, U and bright luminescing Cst II depleted in these elements; Cst III shows the highest CL intensity and enrichment in Ti, V, Ta, Fe, Sb (Fig. 4). The mapping results suggest that Fe and Ti (V)

This is the peer-reviewed, final accepted version for American Mineralogist, published by the Mineralogical Society of America.
The published version is subject to change. Cite as Authors (Year) Title. American Mineralogist, in press.
DOI: https://doi.org/10.2138/am-2022-8200. http://www.minsocam.org/

contents rather than W, Ta and U predominantly govern the luminescence intensity of the Weilasituo cassiterite, or that more complex interactions between elements and site occupancies influence the CL signal. Element maps (Fig. 5) of a Maodeng cassiterite grain show that the distribution of Fe, Ti, V, Sc, Zr and Hf correlates with the oscillatory zoning pattern observed in the CL images (Fig. 3f), while Mn, Nb, Ta, Sb, W, U abundances are all generally low.

4.2. Trace elements geochemistry of cassiterite

A total of 108 cassiterite grains from the three deposits were selected for trace element analysis, the results of which are given in Supplemental Table 2 and plotted in Fig. 6. All cassiterite samples have extremely low Li concentrations, below or near the detection limit. Moreover, U and Cr contents are generally below 20 ppm and 10 ppm, respectively, with the exception of some cassiterite grains from the Maodeng locality that have Cr concentrations up to 36.5 ppm. Iron, Ti and W are sometimes present in significant quantities, with Fe ranging from 21 to 11170 ppm, Ti from 7 to 9714 ppm and W ranging from 3.7 to 9100 ppm. Niobium and Ta contents also vary significantly, from <0.01 up to 5640 ppm for Nb, and up to 511.4 ppm for Ta. Concentrations of other elements also vary by several orders of magnitude, even within a single sample of an ore type (e.g., Al, Sc and Sb). Generally, considering each individual deposit separately, Nb *vs*. U, Fe *vs*. U, Ti *vs*. Sc and Ti *vs*. Zr are positively correlated (Fig. 6a-d), although individual samples from Maodeng deviate from the relevant trend line.

Cassiterites from Weilasituo deposit contain higher Nb, Ta, Zr, Ti, U and Sc contents, but lower Fe, Al, Sb concentrations and Ti/Zr ratios (Fig. 6) than cassiterites from the Baiyinchagan and Maodeng deposits. The Cst II of Weilasituo are characterized by low Fe and W concentrations and mostly plot in the area of SEDEX or VMS tin deposits (e.g., Hennigh and Hutchinson, 1999; Guo et al., 2018) in a W *vs*. Fe diagram (Fig. 6e). In contrast, most other cassiterite grains fall within the range of granite-related tin deposits (e.g., Guo et al., 2018). The Baiyinchagan samples tend to have the highest Fe, Sb and Al contents, and relatively low Nb, Ta and Zr concentrations. They also contain relatively high and variable concentrations of W (30–9100 ppm) and Ti (35–9459 ppm), as well as Ti/Zr values (8–677).

The trace element composition patterns of cassiterite from Maodeng are similar to those from Baiyinchagan, but are generally lower in absolute concentrations. The contents of other elements in cassiterites from the Maodeng samples are among the lowest of the three deposits studied here, excluding Fe, Al, Sb, and Cr. Some elements, including Li, Nb, Ta and U, consistently show concentrations close to, or below their respective detection limits.

4.3. Tin isotope composition

The Sn isotope values for a total of 23 samples are illustrated in Fig. 7, and mean values relative to the in-house standard Sn rod (identical to *SPEX 1*) are listed in Table 2. All isotope results (a total of 204 analysis points) are listed in Supplemental Table 3. The Sn isotope data for cassiterites from Cornwall, Indonesia and Bolivia (Schulze et al., 2017) were added for comparison (Fig. 7d). Mass dependent Sn isotope fractionation is indicated by the slope of $\delta^{122}/^{118}$Sn *vs.* $\delta^{124}/^{117}$Sn (0.57 with r^2=0.99) (Fig. 7).

A significant Sn isotopic variation is observed between the cassiterites from the three tin deposits, with mean $\delta^{124}/^{117}$Sn compositions spanning a range of about 1.25 ‰ (Supplemental Table 3, Fig. 7), translating to a range of 0.17 ‰ per amu. This range is slightly higher than that indicated by experimentally determined isotope fractionation factors (Supplemental Fig.1) (Polyakov et al., 2005) but similar to those observed in earlier studies on tin ores (e.g., Haustein et al., 2010; Brügmann et al., 2017; Yao et al., 2018). The Maodeng cassiterites have the heaviest tin isotopic compositions among the three deposits, with mean $\delta^{124}/^{117}$Sn values range from 0.11 ± 0.04 ‰ to 0.62 ± 0.08 ‰. Compared with the other two deposits, the Sn isotope compositions of Baiyinchagan deposit display the lightest composition, with mean $\delta^{124}/^{117}$Sn values ranging from -1.43 ± 0.06 ‰ to -0.50 ± 0.04 ‰. The range of Sn isotope ratios displayed by the Weilasituo covers that of the other two deposits together with mean $\delta^{124}/^{117}$Sn values ranging from -0.66 ± 0.05 ‰ to 0.59 ± 0.03 ‰.

5. DISCUSSION

5.1. Insight into Sn precipitation mechanism from trace element variations in cassiterite

The ease with which trace elements can be incorporated in cassiterite can be estimated from the divergence of their ionic radius, charge balance, and coordination of ions with

respect to Sn^{4+}, which itself exists in octahedral coordination. Therefore, trace elements that exist as tetravalent cations (e.g., Zr^{4+}, Hf^{4+}) and/or have high octahedral site preference energies (e.g., Cr^{3+}) are relatively compatible in cassiterite. The following trace elements are inferred to be in the following valence states in cassiterite: Al^{3+}, Fe^{3+}, Sc^{3+}, Cr^{3+}, V^{3+}, V^{4+}, Sb^{3+}, Mn^{2+}, Ti^{4+}, Zr^{4+}, Hf^{4+}, W^{4+}, U^{4+}, Nb^{5+}, and Ta^{5+} (Möller et al., 1988; Murciego et al., 1997; Tindle and Breaks, 1998; Cheng et al., 2019; Mao et al., 2020). Some elements may exist in multiple valence states (e.g., W^{4+}/W^{6+}, $V^{3+}/V^{4+}/V^{5+}$, Sb^{3+}/Sb^{5+}), the relative abundance of which reflects the prevailing oxidation state and availability of ligands in the fluid phase from which cassiterite precipitates. For these elements, the lower redox state is likely to predominate in the fluid, because it must be sufficiently reduced so as to solubilize significant quantities of Sn^{2+}. Therefore, trace element concentrations in cassiterite reflect changes in the physical-chemical conditions of the ore-forming fluid. In turn, these may indicate the mechanism by which cassiterite precipitated and the nature of the mineralization (Steveson and Taylor, 1973; Plimer et al., 1991; Murciego et al., 1997; Guo et al., 2018; Cheng et al., 2019). On the whole, the cassiterites from the Weilasituo deposit have high Ta, Nb, W and Zr, which are either incorporated in the mineral lattice or as mineral or fluid inclusions hosted in cassiterite (e.g., Tindle and Breaks, 1998; Guo et al., 2018). The high concentrations of these elements can be attributed to crystallization at high temperature in veins that are proximal to the highly differentiated granitic magmas, already enriched in these elements. In contrast, the enriched Fe-W but depleted Nb-Ta features for Baiyinchagan and Maodeng cassiterites rather indicate a distal low temperature magmatic-hydrothermal origin (e.g., Hennigh and Hutchinson, 1999). Quadrivalent elements can directly substitute for Sn^{4+} as confirmed by the positive correlation between Zr^{4+} and Ti^{4+} (Fig. 6d). Conversely, coupled homogeneous substitution mechanisms have been suggested for the incorporation of trace elements in cassiterite to maintain electro-neutrality, e.g., 2 $(Nb, Ta)^{5+}$ + $(Fe, Mn)^{2+}$ ↔ 3$(Ti, Sn)^{4+}$ (Černý and Ercit, 1985; Möller et al., 1988; Nambaje et al., 2020). However, this mechanism unlikely plays a dominant role for the three deposits studied here due to lack of a good correlation between Fe+Nb+Ta and Ti (Fig. 6g). The cassiterite from Baiyinchagan and Maodeng deposits are characterized by high Fe and W contents which are, however, uncorrelated. Thus, a coupled substitution such as $W^{6+} + 2Fe^{3+} \leftrightarrow 3Sn^{4+}$ (Möller et al., 1988)

415 did not play a leading role in the formation of the cassiterite for these two deposits (Fig. 6e),
416 suggesting instead W was incorporated largely as W^{4+}. As mentioned above, general positive
417 correlations can be observed in binary diagrams of Nb^{5+} *vs.* U^{4+}, Fe^{3+} *vs.* U^{4+}, and Ti^{4+} *vs.*
418 Sc^{3+} for the whole data set including all deposits, suggesting that H^{+} (whose abundance was
419 not determined) may be a significant charge balancing element, as previously proposed
420 (Möller et al., 1988; Cheng et al., 2019; Mao et al., 2020). Furthermore, we noted that Nb
421 was preferentially incorporated compared to Ta in the studied cassiterite grains, which may
422 be explained by the tendency of Nb^{5+} to enter a disordered rutile structure of cassiterite
423 (Möller et al., 1988). Thus, the replacement of Sn^{4+} by Nb^{5+} cannot be completely excluded
424 (Möller et al., 1988; Nambaje et al., 2020).

425 Although some samples display relatively homogeneous CL responses (Fig. 3), the
426 compositional variations observed in the cassiterites are significant and may approach two to
427 three orders of magnitude, e.g., W, U, Zr, Ti, Nb/Ta, etc. (Supplemental Table 2; Fig. 6).
428 Fractionation of these elements by their differential incorporation into cassiterite cannot
429 simply explain the dramatic differences in concentration observed within single cassiterite
430 grains and among investigated samples (Cheng et al., 2019; Mao et al., 2020). Instead, more
431 complex processes, such as elemental fractionation during mineral crystallization as a result
432 of localized fluid disequilibria, or strong changes of fluid compositions within small time
433 intervals after fluid exsoluion, or sluggish element diffusion (due to different diffusivities of
434 trace elements or efficiency of grain boundary diffusion) in the transport medium (e.g.,
435 Koepke and Behrens, 2001; Cheng et al., 2019 and references herein; Mao et al., 2020) would
436 better account for the mechanism responsible for compositional variations. Disequilibrium
437 trace element concentrations due to sluggish element diffusion could be expected in
438 cassiterites crystallizing from silicate melts, but should not occur in cassiterites crystallizing
439 from fluids, which is the case in this study. Such mechanisms would require a change in
440 concentration of >4 orders of magnitude in these elements (Foley et al., 2000; Cheng et al.,
441 2019). Therefore, another explanation is needed. The fluid inclusions studies have revealed
442 the fluid exsoluion processes in the studied tin deposits here (Liu et al., 2018b; Liu, 1996).
443 Moreover, the breccia-related cassiterite mineralization is well developed in Weilasituo,
444 Baiyinchagan and Maodeng deposits, largely due to the relatively shallow emplacement of

the ore-forming granites. Breccia and fracture of the sealed hydrothermal veins could generate channels and spaces for the episodic input of compositionally different ore-forming fluids (Fournier, 1999; Mao et al., 2020), which further support the above mentioned genetic mechanism for the precipitation of cassiterite.

In addition to marked trace element variations, the Cst II of Weilasituo display a distinct compositional range to Cst I. The low Fe and W concentrations of Cst II (Fig. 6e), which are similar to those observed in cassiterites from SEDEX or VMS deposits, may indicate fluid-rock reactions between the mineralizing fluid and surrounding rocks. As tin is commonly transported as a Cl-complex (i.e., $SnCl_2$, $SnCl_3^-$, SnOHCl and $Sn(OH)_2Cl_2$, etc.) in magmatic-hydrothermal fluid systems (Wilson and Eugster, 1990; Wood and Samson, 1998), the partition coefficient of Sn between fluid and melt ($D_{Sn}^{fluid/melt}$) is likely to be governed by the following equilibrium reaction (1) (Heinrich, 1990):

$$[Sn(II)Cl_x]^{2-x}+2H_2O=Sn(IV)O_2+2H^++XCl^-+H_2 \quad (1)$$

The above reaction indicates that cassiterite precipitation is driven by oxidation (H_2 escaping), change in pH, and/or by change in Cl content of the fluid (Heinrich, 1990). In the Weilasituo area, the enrichment of zinnwaldite closely related with cassiterite in quartz (±sulfide) veins hosted by biotite plagioclase gneiss is a possible indication of the interaction of the Sn-bearing fluid with biotite-rich country rocks. As proposed by Eugster (1985), Heinrich (1990) and Nambaje et al. (2020), the reaction of biotite in the host rocks with the mineralizing fluid could lead to the removal of HCl from the Sn fluid and to the formation of zinnwaldite following reaction (2), which may have facilitated the precipitation of Sn as cassiterite Sn (IV) O_2 (Heinrich, 1990):

$$2KFe_3AlSi_3O_{10}(F,OH)_2\ (\textit{biotite})+8HCl+Li_2O+Al_2O_3 = 2KLiFeAl[AlSi_3O_{10}](F,OH)_2\ (\textit{zinnwaldite})+4FeCl_2+3H_2O+H_2 \quad (2)$$

In summary, we conclude that the crystallization of cassiterite from Weilasituo, Baiyinchagan and Maodeng are the products of localized fluid disequilibria or fluids whose compositions change rapidly due to the exsolution of different generations of fluid (e.g., Liu

et al., 2018b; Liu, 1996). Moreover, the significant fluid-rock reactions between ore-forming fluid and surrounding rocks can be seen in the Weilasituo deposit.

5.2. Mechanisms of Sn isotope fractionation

The isotopic variation measured so far in tin ores (e.g., cassiterite, stannite) and some igneous and metamorphic rocks (e.g., granodiorite, peridotite, basalt, komatite) indicates that high-temperature geological processes fractionate Sn isotopes (Yao et al., 2018; Creech et al., 2017; Wang et al., 2018). However, the key processes leading to isotope fractionation of tin during the precipitation of ore-forming fluids, which occur at far lower temperatures (300–500 °C), remain the subject of active investigation (Haustein et al., 2010). The mechanisms by which Sn isotopic fractionation could occur include: 1) equilibrium fractionation between different mineral phases (e.g., cassiterite and stannite (McNaughton and Rosman 1991); 2) equilibrium isotope fractionation between Sn^{2+} and Sn^{4+} complexes between the fluid and precipitating phases controlled by temperature or bond stiffness (e.g., between Sn^{2+} in the fluid and Sn^{4+} in cassiterite, cf. reaction (1)) (Polyakov et al. 2005; Yao et al., 2018; Roskosz et al., 2020; Wang et al., 2021); 3) magmatic fractionation in the course of partial melting or fractional crystallization processes (Creech et al., 2017; Badullovich et al., 2017; Wang et al., 2018); 4) mass-dependent kinetic fractionation through dissolution or precipitation of tin into/from a fluid or melt (Mcnaughton and Loss, 1990; McNaughton and Rosman 1991); 5) liquid-fluid partitioning during exsolution of the fluid phase from its host granitic melt (Mathur et al., 2017; Wang et al., 2019; She et al., 2020).

First, given the geological characteristics of the samples, we can rule out that equilibrium fractionation among the different Sn-bearing mineral phases occurred, because cassiterite is the predominant tin carrier and none or only very little stannite can be found in the three deposits. Experiments at the nickel-nickel oxide (NNO) buffer show that the dissolution of cassiterite is consistent with the presence of $Sn^{2+}Cl_2$ (with $SnCl^+$ and $SnCl_3^-$ becoming more abundant at lower temperatures; Wilson and Eugster, 1990; Müller and Seward, 2001) as the predominant fluid species at 400–700 °C, however, at more oxidizing conditions and under low Cl molarities, hydrated Sn (IV) species also occur, but cassiterite solubility is suppressed (Wang et al., 2021; Schmidt, 2018). Furthermore, if a sulfide phase

506 controlled Sn isotope fractionation, a correlation between the Cu concentrations and δ^{124}Sn in
507 peridotites and basalts may be expected, which is not observed (Wang et al., 2018).
508 Second, due to the consistent variation of Sn isotope values observed for tin ores of
509 deposits that formed in deep vapor-absent environments, Yao et al. (2018) proposed that
510 factors such as variations in pressure and temperature cannot cause the observed fractionation.
511 Moreover, since the main tin mineralization temperatures for each of the three localities are
512 between 300 and 400 ℃ (Korges et al., 2018), temperature does not play a significant role
513 in modifying the reduced isotopic partition function ratios (β-factors), assuming a $10^6/T^2$
514 relationship for 1000 β $^{116/122}$Sn (Supplemental Fig. 2). Furthermore, experimental studies
515 also illustrated that, within the range of pressures typical of the upper continental crust (~ 1
516 GPa) changing pressure does not significantly influence the magnitude of the Sn isotopic
517 fractionation but mostly affects the value of partition coefficients (Roskosz et al., 2020). Our
518 results show that the Sn isotope values of cassiterite formed by magmatic-hydrothermal
519 ore-forming systems at different temperatures largely overlap (Supplemental Table 3, Fig. 7),
520 which also demonstrates that the temperature is not a key factor to isotopic fractionation.
521 Third, the absence of a correlation between the Ta content, Nb/Ta ratios (both indicators
522 of magmatic differentiation because of their extremely low solubility in aqueous fluids;
523 Lehmann, 2020) and tin isotopic values (Supplemental Fig. 3) preclude the possibility of
524 significant isotope fractionation as the result of magmatic differentiation. In contrast, the Sn
525 isotope signatures of the Maodeng (#3) and Baiyinchagan (#2) magmatic-hydrothermal ore
526 systems show a gradual decrease from the early to late mineralization stages (i.e., mean
527 $\delta^{124}/^{117}$Sn values from early to late stages of these two deposits are 0.16 to 0.62 ‰ and 0.11 to
528 0.54 ‰ (#3), -1.25 to -0.50 ‰ and -1.43 to -0.52‰ (#2), respectively) (Table 2), suggesting
529 they were generated by kinetic Rayleigh fractionation during progressive tin ore precipitation,
530 in which the ore-forming fluids become progressively isotopically lighter (e.g., Wilkinson et
531 al., 2005). This interpretation is further supported by the recent transport-precipitation
532 modeling results using first principles molecular dynamics simulations (Wang et al., 2021),
533 which show that heavy Sn isotopes could be removed from fluids under isotopic equilibrium
534 during cassiterite precipitation, because the predominant aqueous species ($SnCl_2$, $SnCl_3^-$)
535 have lower β factors than cassiterite (Polyakov et al., 2005; Wang et al., 2021).

This is the peer-reviewed, final accepted version for American Mineralogist, published by the Mineralogical Society of America.
The published version is subject to change. Cite as Authors (Year) Title. American Mineralogist, in press.
DOI: https://doi.org/10.2138/am-2022-8200. http://www.minsocam.org/

The isotope fractionation of tin may occur in precipitation-dissolution processes within the hydrothermal fluid systems, in which each re-precipitation could come from a fluid with a different isotopic and chemical composition, as well as physicochemical parameters (e.g., fO_2, P-T, and HCl molality) (Graham et al., 2004; Schmidt, 2018). We also note that although the underlying lithologies and tectonic setting are broadly similar for Baiyinchagan and Maodeng deposits (Supplemental Table 1), they display significantly different Sn isotope compositions. Perhaps this effect is supported by different melt compositions at specific deposits (Haustein et al., 2010), since tin mineralization is mainly controlled by magmatic differentiation, source region properties, oxygen fugacity and volatile components (Lehmann, 1990; Heinrich, 1990). The differentiation degree of Baiyinchagan pluton is higher than that of Maodeng intrusion, as indicated by lower bulk rock Nb/Ta, Zr/Hf and K/Rb ratios (2.12–7.50, 4.75–20.49, 27–114 *vs.* 13.34–15.83, 22.02–27.65, 190–240), as well as higher Rb/Sr ratios and F contents (0.30–71.44, 0.13–2.27 wt. % *vs.* 1.03–1.71, 0.09–0.11 wt. %) (Supplemental Table 1). On the other hand, the oxygen fugacity of Baiyinchagan granites are significantly lower than Maodeng rocks (Fig. 2a). All these maybe be responsible for the differences in isotopic composition of these two deposits. In contrast to Maodeng and Baiyinchagan deposits, Weilasituo displays the largest Sn isotopic variability and late-stage cassiterites are characterized by isotopically heavier values than those formed at an early-stage, indicating an overprint by a second pulse of mineralization (see details in Section 5.3).

Finally, recent experimental studies observed that remarkable Sn isotope fractionation can occur during evaporation of Sn chloride solutions at 150℃ ($\triangle^{124}Sn$ = -0.15 ‰, where $\triangle^{124}Sn = \delta^{124}Sn_{solution} - \delta^{124}Sn_{starting\ composition}$) (Wang et al., 2019). Similarly, evaporation experiments performed at 96 ℃ resulted in even larger isotope fractionation ($\triangle^{122/116}Sn$ = -0.36 ‰, $\triangle^{122/118}Sn$ = -0.24 ‰, respectively) (She et al., 2020). The same observations have been made for Zn isotopes of natural samples upon evaporation-condensation processes, with the solid phase being enriched in the heavier isotopes relative to the vapor phase (Cloquet et al., 2008; Moynier et al., 2017). Our results suggest that boiling may cause a wide range of isotope values, explaining the two types of cassiterite (Cst I and Cst II) in the Weilasituo samples (Table 2, Fig. 7) (Liu et al., 2018b). This is also supported by Wang et al. (2019), who found that the range of Sn isotope values for cassiterite is larger if they are formed in

shallow environments which experienced a transition between liquid and vapor, compared to those from cassiterites that formed at greater depth at which only fluid is stable. We infer that liquid-vapor partitioning or vaporization is coupled with strong changes in the physicochemical parameters (e.g., oxygen fugacity, salinity, etc.) of the ore-forming system. For example, fluids from the Weilasituo system have highly variable oxygen fugacities (ΔFMQ – 19.15 ~ ΔFMQ – 3.70; see detailed calculation in Section 5.3) and salinity (4.3–50.9 % NaCleqv.) (Supplemental Table 1; Liu et al., 2018b), which could influence isotopic fractionation of the remaining fluids during the precipitation-dissolution processes of Sn minerals.

It's worth noting that more complex scenarios may require consideration. It is known, for example, that the sources of tin granitic magma may be isotopically heavier than in mantle, which could in turn affect the Sn isotope compositions of cassiterites precipitating from a magmatic-hydrothermal fluid. Furthermore, late stage fluid-rock reaction as well as fluid mixing have the potential to affect Sn isotope compositions of cassiterites. These potential processes are discussed in the following section.

5.3. Tin isotope fractionation during magmatic and hydrothermal processes

Tin granites are mainly derived from partial melting of the crustal material (i.e., they are peraluminous, ilmenite-bearing S-type granites). However, the formation of tin deposits from these granites involves intermediate steps that includes the exsolution of a Sn-bearing fluid phase at magmatic temperatures (~800 °C) and its subsequent cooling to induce cassiterite precipitation (~300 to 500 °C) (Lehmann, 2020). Recently, the USGS reference material, GSP-2 (a *ca*. 1400 Ma granodiorite) yield a $\delta^{124/117}$Sn of 0.61 ‰ relative to the Sn NIST SRM 3161a standard solution (Creech et al., 2017; She et al., 2020). We will use this Sn isotope composition to estimate the starting composition in modelling Sn isotope evolution in our studied samples. The kinetic Sn isotope fractionation factor, α, was determined experimentally as $\alpha_{solution\text{-}solid} = 0.99897$ (She et al., 2020). For the average cassiterite-stannite mineral pair, the calculated $\alpha_{cassiterite\text{-}stannite} = 1.0009$ (i.e., $\alpha_{SnA\text{-}SnB} = (^{heavy}Sn/^{light}Sn)_{SnA} / (^{heavy}Sn/^{light}Sn)_{SnB}$) based on the Sn isotope data from Yao et al. (2018). With the aim of predicting the range of fluids that would evolve from a granitic magma and the composition

of the precipitating phase, we apply a Rayleigh distillation model using Eq. (3) (She et al., 2020) to address this issue.

$$\frac{\ln\left(\left(1000+\delta_f\right)/\left(1000+\delta_i\right)\right)}{\ln\left(F\right)}=\left(\alpha-1\right) \quad (3)$$

where δ_i and δ_f are the Sn isotopic values of the initial Sn solution and the residual Sn in metal precipitate, respectively. F is a proportion of Sn in magma/ Sn in fluid.

This modeling indicates that nearly the first 90% (Fig. 8) of Sn that precipitated from such a hydrothermal fluid would have $\delta^{124/117}$Sn = -1.41 ‰ to 1.49 ‰ (isotope values are converted relative to the Sn standard NIST SRM 3161a, using the cross-calibration of Yamazaki et al. (2013), Brügmann et al. (2017) and She et al. (2020) according to Eq. (4).

$$\delta^{124/117}Sn_{3161a}=\delta^{124/117}Sn_{\text{Tin rod}}+0.54 \quad (4)$$

This is in agreement with the distribution of Sn isotope values for cassiterites from tin deposits in NE China in Supplemental Table 3. Moreover, this result is consistent with that of Yao et al. (2018) based on Rayleigh distillation modeling for tin ores from the Cornwall, Erzgebirge and Bolivia. Our model also indicates that in order to obtain solutions and solids fitting our isotope results, more than ~95% of all Sn in the system must have precipitated in the form of cassiterite (Fig. 8). This is consistent with the relative abundance of cassiterite and stannite in tin ores globally (Lehmann, 1990).

Degree of fractionation (mainly controlled by fractional crystallization) and oxidation state are the two particularly crucial factors for magmatic Sn enrichment in granite bodies (Lehmann, 2020). Based on Sn isotope investigations of magmatic standards and samples from Kilauea Iki (Hawaii), Badullovich et al. (2017) proposed that Sn isotopes remain essentially unfractionated during fractional crystallization of silicates, because Sn is incompatible in most silicates, but decrease to lighter values in the melt along with ilmenite precipitation. They proposed that Sn isotope fractionation during ilmenite crystallization is driven by the incorporation of Sn^{4+} into ilmenite, i.e. by the coordination variation between

625 Sn^{4+} in the melt (6- to 8-fold) and ilmenite (6-fold), as proved by lattice strain modelling.
626 This view was supported by an experimental study of Roskosz et al. (2020), who determined
627 the force constant of tin bonds in basalt, rhyolite, enstatite and anorthite glasses by using
628 synchrotron nuclear resonance inelastic X-ray scattering (NRIXS) so as to determine the β-
629 factors of these glasses. The conclusions of Roskosz et al. (2020) are also consistent with the
630 isotope fractionation theory based on vibrational frequencies (Schauble, 2004), which
631 indicates that heavy Sn isotopes will be preferentially incorporated into Sn^{4+} bondings (as Sn
632 (IV)-O has much shorter bond length (~2.18 Å) than Sn (II)-S (~2.48 Å)) and accordingly
633 enriched in the melt during partial melting (since Sn^{4+} behaves more incompatible during
634 mantle melting), but depleted in the melt during ilmenite crystallization (Wang et al., 2018;
635 Gürel et al., 2011; Roskosz et al., 2020).

636 The cassiterite samples analysed here show that the isotopically heaviest cassiterite is
637 from Maodeng deposit, which formed from the granitic magma with less differentiation but
638 higher oxygen fugacity among the three deposits (Supplemental Table 1). This is in
639 agreement with the above scenario of magmatic Sn isotope fractionation. On the other hand,
640 the Weilasituo samples, related to a highly fractionated magma, display a range in $\delta^{124/117}Sn$
641 from -1.49 to 0.85 ‰ (Supplemental Table 3, Fig. 7), which is the largest range among the
642 three deposits. Furthermore, the Sn isotope ratios of the late ore-forming stage are heavier
643 than that in the early stage. This latter finding cannot be explained by magmatic fractionation
644 and related source heterogeneities alone. First of all, cassiterite has a high density of 7.15
645 g/cm^{-3} and is mechanically and chemically resistant (Haustein et al., 2010; Lehmann, 2020).
646 Thus, terrestrial weathering seems not to significantly affect Sn isotopic compositions or Sn
647 contents (Braukmüller et al., 2018; Creech and Moynier, 2019). This means that the
648 epigenetic processes after mineralization most likely do not affect the Sn isotopic ratios of tin
649 ores.

650 Tin has three valence states (i.e., Sn^0, Sn^{2+}, Sn^{4+}) so its geochemical behavior is strongly
651 influenced by oxygen fugacity (Linnen et al., 1996; Badullovich et al., 2017), and
652 considerable Sn isotope fractionations are expected during redox processes (Polyakov et al.,
653 2005; Yao et al., 2018; Wang et al., 2018; Dauphas et al., 2017). To evaluate redox condition
654 of the cassiterite samples, we calculated the oxygen fugacity of the ore fluid of individual tin

deposits based on bulk-rock and trace element data of zircon (Gao et al., 2019; Yao et al., 2017; Guo et al., 2019), using the Geo-fO_2 software (Li et al., 2019). The results show that oxygen fugacity and Sn isotope ratios covary. For example, the Weilasituo deposit displays the largest range of Sn isotope compositions and oxygen fugacity, whereas the Maodeng deposit possesses the heaviest Sn isotope values and the highest oxygen fugacity. Although this is not particularly diagnostic, it may suggest that changes in oxygen fugacity can cause significant Sn isotope fractionation. Furthermore, it has been proved that anomalously high isotope values may indicate late-magmatic fluid-rock interaction with external, wall rock-derived fluids, for example, Cu, Zn isotopes (e.g., Liu et al., 2019). Our previous studies have shown that, in the Weilasituo deposit, the oxygen fugacity of the fluid derived from the surrounding rocks (biotite plagioclase gneiss) is several orders of magnitude higher than that of the early magmatic-hydrothermal fluid (Gao et al., 2019). The Weilasituo tin granites are characterized by a notable REE tetrad effect and high TE_{1-3} (Fig. 2b), as well as the enrichment of transition metals (e.g., Sc, Ti, Cr, etc.) in cassiterite (Supplemental Table 2), which indicate fluid-rock interaction with an external metamorphic fluid (e.g., Erber, 1999; Jiang et al., 2004). This may explain the heavy Sn isotopic values of late stage cassiterite, which may have been generated by reaction with an isotopically heavy Sn^{4+} rich fluid derived from wall rocks. However, more experimental studies focusing on fractionation mechanism of tin at high temperatures (>300℃) (e.g., Wang et al., 2021), such as fluid-rock reaction and continual dissolution-precipitation are needed.

5.4. Exploration potential and implications of Sn isotope signatures

Tin, W or Sn-W mineralization are generally hosted in metasomatized roof zones (greisen) and/or quartz veins, which can be developed proximal to the intrusion, or may extend to more distal areas into the wall rocks (Korges et al., 2018). Previous studies proposed that the Ti/Zr ratios of cassiterite are likely to decrease with distance away from the granite intrusion, which would be related to a progressive decrease of Ti concentrations relative to Zr in the fluid because it migrated and evolved away from the intrusion (e.g., Kessel et al., 2005; Cheng et al., 2019). In our cases, there are no Ti- or Zr-rich minerals associated with any of the ore mineral assemblages studied here, so the fractionation of Ti/Zr

by co-existing hydrothermal mineral phases can be ignored (Cheng et al., 2019). The Ti/Zr ratios of Baiyinchagan and Maodeng cassiterites are highly variable, which could indicate that the cassiterites formed from different distances to the related granite intrusion. These variable Ti/Zr ratios of cassiterite in deposits are strongly positively correlated with the Sn isotope ratios (Fig. 9), implying that $\delta^{124}/^{117}$Sn of the fluid may have been fractionated toward lower values during progressive fluid evolution, similar to Ti/Zr ratios. This finding highlights the possible use of Sn isotopes as an effective tool to reconstruct fluid pathways in a tin mineralization system associated with granites. Moreover, as the Maodeng and Baiyinchagan deposits share a similar tectonic setting and ore-bearing strata, but cover different ranges of tin isotopic compositions (Supplemental Tables 1 and 3; Fig. 1, 7) and a distinct offset of the $\delta^{124}/^{117}$Sn *vs.* Ti/Zr correlation (Fig. 9). These findings indicate that Sn isotope compositions may be significantly affected by different isotopic signatures of the Sn source, i.e. of the initial granitic melt.

As mentioned above, Sn is known to have high affinity to Cl to form tin chloride, but the dominant speciation of Sn (II/IV)-Cl complexes in hydrothermal fluids remains controversial topic, e.g., stability of Sn (IV) species (i.e., $SnCl_6^{2-}$, $SnCl_5(H_2O)^-$, $SnCl_4(H_2O)_2$, etc.) in aqueous solutions has been revealed using various methods (Sherman et al., 2000; Schmidt, 2018; She et al., 2020); however, numerous previous studies did report stability of Sn (II) species (i.e., $SnCl^{3-}$, $SnCl_2(H_2O)$, $SnCl(H_2O)_2^+$, etc.) under hydrothermal conditions (Wilson and Eugster, 1990; Müller and Seward, 2001; Duc-Tin et al., 2007). More recently, Wang et al. (2021) and She et al. (2020) applied first principle methods to constrain the speciation of Sn (II/IV)-Cl complexes in hydrothermal fluids and the corresponding Sn isotope effects, which provide a physical basis for understanding the transport and mineralization of Sn. Our Sn isotope data measured from separate mineral deposits with specific paragenetic constraints, together with previous studies of fluid inclusions (Liu et al., 2018b; Liu et al., 1996; Yao et al., 2017), allow us to investigate the Sn speciation during cassiterite precipitation in mineralizing systems. Based on the continuous transport-precipitation model (Wang et al., 2021) (Fig. 10), we can estimate the Sn (II) species had existed in early tin mineralization systems, then shifted to Sn (IV) species in late stage due to redox change or higher Cl^- activity (Wang et al., 2021). This is supported by fluid inclusion studies on Sn deposits. For

example, Liu et al. (2018b) reported high salinity (up to 50.9 wt.% NaCl equiv.) in early ore-forming fluids from the Weilasituo tin deposit. As the Sn^{4+} coordinates with more Cl^- compare to Sn^{2+}, the higher Cl^- activity can enhance the conversion to Sn (IV)-Cl complexes, which can facilitate the formation of tin deposits, considering the crystal chemistry of cassiterite (Wang et al., 2021). The solubility experiments from 400 ℃ to 800 ℃ have showed that $SnCl_2$ was the dominant species in supercritical aqueous fluids (Wilson and Eugster, 1990; Duc-Tin et al., 2007). Furthermore, the cassiterite trace element data combined with highly variable oxygen fugacities show the effects of redox reactions on the Sn isotope fractionation (c.f., Yao et al., 2018). Consequently, the Sn isotope studies can provide insight into understanding the mechanistic details of hydrothermal Sn mineralization.

With the purpose of understanding the direct relationship between Sn isotope behavior and tin mineralization, a complementary dataset (Supplemental Table 4) (e.g., Haustein et al., 2010; Brügmann et al., 2017; Wang et al., 2018; Yao et al., 2018; Wang et al., 2019) comprising reliable Sn isotope compositions of tin ores from different geological backgrounds has been compiled. This data compilation shows (Fig. 11) that the Sn isotope composition of cassiterites from deposits that formed at different ages (from Precambrian to Cenozoic) and tectonic settings (e.g., subduction, continental collision, and anorogenic extension environment) largely overlap, indicating that no direct relationship between the Sn isotope composition and ages or tectonic background exists. The late Paleozoic cassiterites, mostly from the Erzgebirge and Cornwall, show the largest range of Sn isotope compositions, which may be due to the fact that they mostly belong to greisen type deposits, and the mineralization process experienced significant fluid-rock interaction (Jackson et al., 1989; Wilkinson et al., 1995; Breiter et al., 2017, 2019). Moreover, cassiterite seems to display heavier Sn isotopes relative to coexisting stannite, independent of deposit type and depth of emplacement (Fig. 10). This isotope shift is likely generated during the oxidation of tin in solution, as experimental data has proved that Sn^{4+} is enriched in heavy isotopes relative to Sn^{2+} (Polyakov et al., 2005; Wang et al., 2018; Roskosz et al., 2020). The precipitation of heavy-Sn-enriched cassiterite results in residual dissolved Sn with lighter isotope compositions of later-formed stannite (Yao et al., 2018). In addition, the cassiterites as placer-tin from different mining areas show a narrow range of Sn isotope ratios, which seems

745 not to be inherited from the protoliths (crust material) and slightly heavier than the estimated
746 Sn isotope composition of BSE (Wang et al., 2018). This offset may reflect the Sn isotope
747 composition of the external fluid (e.g., mantle slab-derived fluid with high oxygen fugacity)
748 involved during crustal melting (e.g., Mungall, 2002) but more research is needed to
749 elucidate this issue.
750
751 **6. CONCLUSION**
752 In this contribution, the first high-precision *in situ* Sn isotope measurements of
753 cassiterites from individual tin deposits were obtained using UV-*fs*-LA-ICPMS. Our studies
754 on Sn isotope signatures of the Maodeng and Baiyinchagan magmatic-hydrothermal ore
755 systems have shown that isotope values gradually decrease from the early to late
756 mineralization stages, suggesting they were generated by kinetic Rayleigh fractionation
757 during progressive precipitation of tin ores from hydrothermal fluids. Elevated Sn isotope
758 values in the Weilasituo cassiterite from the late stage are likely a result of disequilibrium
759 fluid-rock interaction. Combining the Sn isotope ratios with their trace element composition
760 (e.g., Fe, W, Ti, Zr, etc.) furthermore suggests that the ores formed from localized
761 dynamically-evolving fluids, and supports the contention that significant fluid-rock reaction
762 occurred in Weilasituo. The findings of our study imply that processes such as liquid-vapor
763 partitioning or vaporization, and fluid-rock interaction have a much greater effect on Sn
764 isotope fractionation than does magmatic differentiation in tin deposits. Altogether, the Sn
765 isotopes may be a robust tool to trace the ore mineralization center and fluid pathways, as
766 well as to ascertain the mechanisms of metal precipitation, which may aid mineral
767 exploration.
768
769 **ACKNOWLEDGEMENTS**
770 This work is funded by the National Natural Science Foundation of China (No.
771 41772084, and 41820104010), the National Key R&D Program of China (No.
772 2019YFC0605202), and the Science & Technology Basic Resources Investigation Program of
773 China (No. 2017FY101300 and 2017FY101302). We acknowledge Wentao Zhao, Boyang Li,
774 Dawei Jiang, Xu Fu, Kexiang Wang and Hucan Jiang for their help during field trip. The

author thanks Dr. Maria Kirchenbaur, Prof. Junming Yao and Prof. Chao Li for helpful discussions. We also thank Dr. Antony Burnham for assistance in English polishing and manuscript improvement. This study benefited from constructive comments from Dr. Maria Alejandra Rodriguez Mustafa and one anonymous reviewer, as well as editorial handing from associate editor Prof. Paul Tomascak.

REFERENCES

Badullovich, N., Moynier, F., Creech, J.B., Teng, F.Z., and Sossi, P.A. (2017) Tin isotopic fractionation during igneous differentiation and Earth's mantle composition. Geochemical Perspective Letters, 5, 24−28.

Braukmüller, N., Wombacher, F., Hezel, D.C., Escoube, R., and Münker, C. (2018) The chemical composition of carbonaceous chondrites: implications for volatile element depletion, complementarity and alteration. Geochimica et Cosmochimica Acta, 239, 17−48.

Breiter, K., Ďurišová, J., and Dosbaba, M. (2017) Quartz chemistry – A step to understanding magmatic-hydrothermal processes in ore-bearing granites: Cínovec/Zinnwald Sn-W-Li deposit, Central Europe. Ore Geology Reviews, 90, 25−35.

Breiter, K., Hložková, M., Korbelová, Z., and Galiová, M.V. (2019) Diversity of lithium mica compositions in mineralized granite–greisen system: Cínovec Li-Sn-W deposit, Erzgebirge. Ore Geology Reviews, 106, 12−27.

Brügmann, G., Berger, D., and Pernicka, E. (2017) Determination of the tin stable isotopic composition in tin-bearing metals and minerals by MC-ICP-MS. Geostandards and Geoanalytical Research, 41, 437−448.

Černý, P., and Ercit, T.S. (1985) Some recent advances in the mineralogy and geochemistry of Nb and Ta in rare-element granitic pegmatites. Bulletin De Mineralogie, 108, 499−532.

Černý, P., Blevin, P.L., Cuney, M., and London, D. (2005) Granite-related ore deposits. In: Hedenquist, J.W., Thompson, J.F.H., Goldfarb, R.J. and Richards, J.P. (eds), Economic geology 100th anniversary volume (1905–2005), Society of Economic Geologists. Society of Economic Geologists (Littleton, CO), 337−370.

Cheng, Y.B., Spandler, C., Kemp, A., Mao, J.W., Rusk, B., Hu, Y., and Blake, K. (2019) Controls on cassiterite (SnO_2) crystallization: Evidence from cathodoluminescence, trace-element chemistry, and geochronology at the Gejiu Tin District. American Mineralogist, 104, 118−129.

Clayton, R., Andersson, P., Gale, N.H., Gillis, C., and Whitehouse, M.J. (2002) Precise determination of the isotopic composition of Sn using MC-ICP-MS. Journal of Analytical Atomic Spectrometry, 17, 1248−1256.

Cloquet, C., Carignan, J., Lehmann, M., and Vanhaecke, F. (2008) Variation in the isotopic composition of zinc in the natural environment and the use of zinc isotopes in biogeosciences: a review. Analytical and Bioanalytical Chemistry, 390, 451−463.

Creech, J.B., Moynier, F., and Badullovich, N. (2017) Tin stable isotope analysis of geological materials by double-spike MC-ICPMS. Chemical Geology, 457, 61−67.

Creech, J.B. and Moynier, F. (2019a) Tin and zinc stable isotope characterisation of chondrites and implications for early Solar System evolution. Chemical Geology, 511, 81−90.

Creech, J.B., Moynier, F., and Koeberl, C. (2019b) Volatile loss under a diffusion-limited regime in tektites: Evidence from tin stable isotopes. Chemical Geology, 528, 119279.

Dauphas, N., Roskosz, M., Alp, E.E., Neuville, D.R., Hu, M.Y., Sio, C.K., Tissot, F.L.H., Zhao, J., Tissandier, L., Médard, E., and Cordier, C. (2014) Magma redox and structural controls on iron isotope variations in Earth's mantle and crust. Earth and Planetary Science Letters, 398, 127−140.

Dauphas, N., John, S.G., and Rouxel, O. (2017) Iron isotope systematics. Reviews in Mineralogy Geochemistry, 82, 415−510.

De Laeter, J.R.D., and Jeffery, P.M. (1965) The isotopic composition of terrestrial and meteoritic tin. Journal of Geophysical Research, 70, 2895−2903.

De Laeter, J.R.D., and Jeffery, P.M. (1967) Tin: its isotopic and elemental abundance. Geochimica et Cosmochimica Acta, 31, 969−985.

Duc-Tin, Q., Audétat, A., and Keppler, H. (2007) Solubility of tin in (Cl, F)-bearing aqueous fluids at 700 ℃, 140 MPa: a LA-ICPMS study on synthetic fluid inclusions. Geochimica et Cosmochimica Acta, 71, 3323−3335.

Eugster, H.P. (1985) Granites and hydrothermal ore-deposits—A geochemical framework. Mineralogical Magazine, 49, 7−23.

Farmer, C.B., Searl, A., and Halls, C. (1991) Cathodoluminescence and growth of cassiterite in the composite lodes at South Crofty Mine, Cornwall, England. Mineralogical Magazine, 55, 447−458.

Foley, S.F., Barth, M.G., and Jenner, G.A. (2000) Rutile/melt partition coefficients for trace elements and an assessment of the influence of rutile on the trace element characteristics of subduction zone magmas. Geochimica et Cosmochimica Acta, 64, 933–938.

Fournier, R.O. (1999) Hydrothermal processes related to movement of fluid from plastic into brittle rock in the magmatic-epithermal environment. Economic Geology 94, 1193−1211.

Gao, X., Zhou, Z.H., Breiter, K., Ouyang, H.G., and Liu, J. (2019) Ore formation mechanism of the Weilasituo tin-polymetallic deposit, NE China: Constraints from bulk-rock and mica chemistry, He-Ar isotopes, and Re-Os dating. Ore Geology Reviews, 109, 163−183.

Graham, S., Pearson, N., Jackson, S., Griffin, W., and O'Reilly, S.Y. (2004) Tracing Cu and Fe from source to porphyry: in situ determination of Cu and Fe isotope ratios in sulfides from the Grasberg Cu-Au deposit. Chemical Geology, 207, 147−169.

Guo, J., Zhang, R.C., Sun, W.D., Ling, M.X., Hu, Y.B., Wu, K., Luo, M., and Zhang, L.C. (2018) Genesis of tin-dominant polymetallic deposits in the Dachang district, South China: Insights from cassiterite U-Pb ages and trace element compositions. Ore Geology Reviews, 95, 863−879.

Guo, S., He, P., Zhang, X.B., Cui, Y.R., Zhang, T.F., Zhang, K., Lai, L., and Liu, C.B. (2019) Geochronology and geochemistry of Maodeng-Xiaogushan tin-polymetallic ore-field in southern Da Hinggan Mountains and their geological significances. Mineral Deposits, 38, 509−525 (in Chinese with English abstract).

Günther, T., Klemd, R., Zhang, X., Horn, I., and Weyer, S. (2017) In-situ trace element and Fe-isotope studies on magnetite of the volcanic-hosted Zhibo and Chagangnuoer iron ore

deposits in the Western Tianshan, NW China. Chemical Geology, 453, 111−127.

Gürel, T., Sevik, C., and Cağin, T. (2011) Characterization of vibrational and mechanical properties of quaternary compounds Cu_2ZnSnS_4 and $Cu_2ZnSnSe_4$ in kesterite and stannite structures. Physical Review Letters, B84, 205201.

Hall, M.R., and Ribbe, P.H. (1971) An electron microprobe study of luminescence centers in cassiterite. American Mineralogist, 56, 31−45.

Haustein, M., Gillis, C., and Pernicka, E. (2010) Tin isotopy—A new method for solving old questions. Archaeometry, 52, 816−832.

Heinrich, C.A. (1990) The chemistry of hydrothermal tin (-tungsten) ore deposition. Economic Geology, 85, 457−481.

Hennigh, Q., and Hutchinson, R.W. (1999) Cassiterite at Kidd Creek: an example of volcanogenic massive sulfide-hosted tin mineralization. Economic Geology, 10, 431−440.

Horn, I., von Blanckenburg, F., Schoenberg, R., Steinhoefel, G. and Markl, G., (2006) In situ iron isotope ratio determination using UV-femtosecond laser ablation with application to hydrothermal ore formation processes. Geochimica et Cosmochimica Acta, 70, 3677−3688.

Horn, I., and von Blanckenburg, F. (2007) Investigation on elemental and isotopic fractionation during 196 nm femtosecond laser ablation multiple collector inductively coupled plasma mass spectrometry. Spectrochimica Acta Part B, 62, 410−422.

Hu, M.Y., Toellner, T.S., Sturhahn, W., Hession, P. M., Sutter, J.P. and Alp, E.E. (1999) A high-resolution monochromator for inelastic nuclear resonant scattering experiments using ^{119}Sn. Nuclear Instruments & Methods, A430, 271−277.

Irber, W. (1999) The lanthanide tetrad effect and its correlation with K/Rb, Eu/Eu*, Sr/Eu, Y/Ho, and Zr/Hf of evolving peraluminous granite suites. Geochimica et Cosmochimica Acta, 63, 89−508.

Jackson, N., Willis-Richards, J., Manning, D., and Sams, M. (1989) Evolution of the Cornubian ore field, Southwest England: Part II. Mineral deposits and ore-forming processes. Economic Geology, 84, 1101−1133.

Jiang, S.Y., Yu, J.M., and Lu, J.J. (2004) Trace and rare-earth element geochemistry in tourmaline and cassiterite from the Yunlong tin deposit, Yunnan, China: implication for migmatitic–hydrothermal fluid evolution and ore genesis. Chemical Geology, 209, 193−213.

Keith, M., Haase, K.M., Schwarz-Schampera, U., Klemd, R., Petersen, S., and Bach, W. (2014) Effects of temperature, sulfur, and oxygen fugacity on the composition of sphalerite from submarine hydrothermal vents. Geology, 42, 699−702.

Kessel, R., Ulmer, P., Pettke, T., Schmidt, M.W., and Thompson, A.B. (2005) The water-basalt system at 4 to 6 GPa: Phase relations and second critical endpoint in a K-free eclogite at 700 to 1400 °C. Earth and Planetary Science Letters, 237, 873−892.

Koepke, J., and Behrens, H. (2001) Trace element diffusion in andesitic melts: An application of synchrotron X-ray fluorescence analysis. Geochimica et Cosmochimica Acta, 65, 1481−1489.

Korges, M., Weis, P., Lüders, V., and Laurent, O. (2018) Depressurization and boiling of a single magmatic fluid as a mechanism for tin-tungsten deposit formation. Geology, 46, 75−78.

Lehmann, B. (1990) Metallogeny of Tin. Springer-Verlag, Berlin (211 pp.).

Li, W., Jackson, S.E., Pearson, N.J., Alard, O., and Chappell, B.W. (2009) The Cu isotopic signature of granites from the Lachlan Fold Belt, SE Australia. Chemical Geology, 258, 38−49.

Li, W.K., Cheng, Y.Q. and Yang, Z.M. (2019). Geo-fO_2: Integrated software for analysis of magmatic oxygen fugacity. Geochemistry Geophysics Geosystems, 20, 2542−2555.

Linnen, R.L., Pichavant, M., and Holtz, F. (1996) The combined effects of fO_2 and melt composition on SnO_2 solubility and tin diffusivity in haplogranitic melts. Geochimica et Cosmochimica Acta, 60, 4965−4976.

Liu, P., Mao, J.W., Lehmann, B., Weyer, S., Horn, I., Mathur, R., Wang, F.Y. and Zhou, Z.H. (2021). Tin isotopes *via* fs-LA-MC-ICP-MS analysis record complex fluid evolution in single cassiterite crystals. American Mineralogist, in press.

Liu, R.L., Wu, G., Li, T.G., Chen, G.Z., Wu, L.W., Zhang, P.C., Zhang, T., Jiang, B., and Liu, W.Y. (2018a) LA-ICP-MS cassiterite and zircon U-Pb ages of the Weilasituo tin-polymetallic deposit in the southern Great Xing'an Range and their geological significance. Earth Science Frontiers, 25, 183−201 (in Chinese with English abstract).

Liu, R.L., Wu, G., Chen, G.Z., Li, T.G., Jiang, B., Wu, L.W., Zhang, P.C., Zhang, T., and Chen, Y.C. (2018b) Characteristics of fluid inclusions and H-O-C-S-Pb isotopes of Weilasituo Sn-polymetallic deposit in southern Da Hinggan Mountains. Mineral Deposits, 37, 199−224 (in Chinese with English abstract).

Liu, S.A., Liu, P.P., Lv, Y.W., Wang, Z.Z., and Dai, J.G. (2019) Cu and Zn isotope fractionation during oceanic alteration: Implications for Oceanic Cu and Zn cycles. Geochimica et Cosmochimica Acta, 257, 191−205.

Liu, X., Wang, J.B., Zhu, X.Y., Sun, Y.L., Jiang, H.Y., Jiang, B.B., Wang, H., and Cheng, X.Y. (2017) Mineralization process of the Baiyinchagan tin polymetallic deposit in Inner Mongolia I: Metallic mineral assemblage and metallogenic mechanism. Mineral Exploration, 8, 967−980 (in Chinese with English abstract).

Liu, Y.Q. (1996) Metallogenic zoning and origin of the Maodeng tin-copper deposit. Mineral Deposits, 15, 318−329 (in Chinese with English abstract).

Mao, J.M., Ouyang, H.G., Song, S.W., Santosh, M., Yuan, S.D., Zhou, Z.H., Zheng, W., Liu, H., Liu, P., Cheng, Y.B. and Chen, M.H. (2019) Geology and metallogeny of tungsten and tin deposits in China. Economic Geology, Special Publications, 411−482.

Mao, W., Zhong, H., Yang, J.H., Tang, Y.W., Liu, L., Fu, Y.Z., Zhang, X.C., Sein, K., Aung, S.M., Li, J., and Zhang, L. (2020) Combined zircon, molybdenite, and cassiterite geochronology and cassiterite geochemistry of the Kuntabin tin-tungsten deposit in Myanmar. Economic Geology, 115, 603−625.

Marechal, C.N., Telouk, P., and Albarede, F. (1999) Precise analysis of copper and zinc isotopic compositions by plasma-source mass spectrometry. Chemical Geology, 156, 251−273.

Mason, A.H., Powell, W.G., Bankoff, H.A., Mathur, R., Price, M., Bulatovic, A., and Filipovic, V. (2020) Provenance of tin in the Late Bronze Age Balkans based on probabilistic and spatial analysis of Sn isotopes. Journal of Archaeological Science, 122, 105−181.

Mathur, R., Titley, S., Barra, F., Brantley, S., Wilson, M., Phillips, A., Munizaga, F., Maksaev,

V., Vervoort, J., and Hart, G. (2009) Exploration potential of Cu isotope fractionation in porphyry copper deposits. Journal of Geochemical Exploration, 102, 1−6.

Mathur, R., Powell, W., Mason, A., Godfrey, L., Yao, J.M., and Baker, M.E. (2017) Preparation and measurement of cassiterite for Sn isotope analysis. Geostandards and Geoanalytical Research, 41, 701−707.

Mcnaughton, N.J., and Loss, R.D. (1990) Stable isotope variations of tin. In Stable Isotopes and Fluid Processes in Mineralization (eds. Herbert, H.K., and Ho, S.E.). Geol. Dept. & Univ. Ext. Univ. Western Australia Publication, 23, 269−276.

Mcnaughton, N.J., and Rosman, K.J.R. (1991) Tin isotope fractionation in terrestrial cassiterites. Geochimica et Cosmochimica Acta, 55, 499−504.

Meija, J., Coplen, T.B., Berglund, M., Brand, W.A., De, B.P., Gröning, M., Holden, N.E., Irrgeher, J., Loss, R.D., Walczyk, T., and Prohaska, T. (2016) Isotopic compositions of the elements 2013 (IUPAC technical report). Pure Applied Chemistry, 88, 293−306.

Möller, P., Dulski, P., Szacki, W., Malow, G., and Riedel, E. (1988) Substitution of tin in cassiterite by tantalum, niobium, tungsten, iron and manganese. Geochimica et Cosmochimica Acta, 52, 1497−1503.

Moynier, F., Vance, D., Fujii, T., and Savage, P. (2017) The isotope geochemistry of zinc and copper. Reviews in Mineralogy & Geochemistry, 82, 543−600.

Müller, B., and Seward, T.M. (2001). Spectrophotometric determination of the stability of tin(II) chloride complexes in aqueous solution up to 300°C. Geochimica et Cosmochimica Acta, 65, 4187−4199.

Mungall, J.E. (2002) Roasting the mantle: Slab melting and the genesis of major Au and Au-rich Cu deposits. Geology, 30, 915−918.

Murciego, A., Sanchez, A.G., Dusausoy, Y., Pozas, J.M.M., and Ruck, R. (1997) Geochemistry and EPR of cassiterites from the Iberian Hercynian Massif. Mineralogical Magazine, 61, 357−365.

Nambaje, C., Eggins, S.M., Yaxley, G.M., and Sajeev, K. (2020) Micro-characterisation of cassiterite by geology, texture and zonation: A case study of the Karagwe Ankole Belt, Rwanda. Ore Geology Reviews, 124, 103609.

Paton, C., Hellstrom, J., Paul, B., Woodhead, J., and Hergt, J. (2011) Iolite: Freeware for the visualisation and processing of mass spectrometric data. Journal of Analytical Atomic Spectrometry, 26, 2508−2518.

Plimer, I.R., Lu, J., and Kleeman, J.D. (1991) Trace and rare earth elements in cassiterite—sources of components for the tin deposits of the Mole Granite, Australia. Mineralium Deposita, 26, 267−274.

Polyakov, V.B., Mineev, S.D., Clayton, R.N., Hu, G., and Mineev, K.S. (2005) Determination of tin equilibrium isotope fractionation factors from synchrotron radiation experiments. Geochimica et Cosmochimica Acta, 69, 5531−5536.

Roskosz, M., Amet, Q., Fitoussi, C., Dauphas, N., Bourdon, B., Tissandier, L., Hu, M.Y., Said, A., Alatas, A., and Alp, E.E. (2020) Redox and structural controls on tin isotopic fractionations among magmas. Geochimica et Cosmochimica Acta, 268, 42−55.

Russell, W.A., Papanastassiou, D.A., and Tombrelu, T.A. (1978) Ca isotope fractionation on the earth and other solar system materials. Geochimica et Cosmochimica Acta, 42, 1075−1090.

Schauble, E.A. (2004) Applying stable isotope fractionation theory to new systems. Reviews in Mineralogy and Geochemistry, 55, 65−111.

Schmidt, C. (2018) Formation of hydrothermal tin deposits: Raman spectroscopic evidence for an important role of aqueous Sn (IV) species. Geochimica et Cosmochimica Acta, 220, 499−511.

Schulze, M., Ziegerick, M., Horn, I., Weyer, S., and Vogt, C. (2017) Determination of tin isotope ratios in cassiterite by femtosecond laser ablation multicollector inductively coupled plasma mass spectrometry. Spectrochimica Acta, B 130, 26−34.

She, J.X., Wang, T.H., Liang, H.D., Muhtar, M.N., Li, W.Q., and Liu, X.D. (2020) Sn isotope fractionation during volatilization of Sn (IV) chloride: laboratory experiments and quantum mechanical calculations. Geochimica et Cosmochimica Acta, 269, 184−202.

Sherman, D.M., Ragnarsdottir, K.V., Oelkers, E.H., and Collins, C.R. (2000) Speciation of tin (Sn^{2+} and Sn^{4+}) in aqueous Cl solutions from 25 ℃ to 350 ℃: an in situ EXAFS study. Chemical Geology, 167, 169−176.

Shi, G.H., Liu, D.Y., Zhang, F.Q., Jian, P., Miao, L.C., Shi, Y.R., and Tao, H. (2003) SHRIMP U-Pb zircon geochronology and its implications on the Xilin Gol Complex, Inner Mongolia, China. Chinese Science Bulletin, 48, 2742−2748.

Sossi, P.A., Nebel, O., O'Neill, H.S.C., and Moynier, F. (2018) Zinc isotope composition of the earth and its behaviour during planetary accretion. Chemical Geology, 477, 73−84.

Steveson, B.G., and Taylor, R.G. (1973) Trace element content of some cassiterites from Eastern Australia. Proceed. R. Soc. Queensland 84, 43−54.

Thompson, J., Meffre, S., and Danyushevsky, L. (2018) Impact of air, laser pulse width and fluence on U-Pb dating of zircons by LA-ICPMS. Journal of Analytical Atomic Spectrometry, 33, 221−230.

Teng, F.Z., Dauphas, R.T., Helz, R.T. (2008) Iron isotope fractionation during magmatic differentiation in Kilauea Iki Lave Lake. Science, 320, 1620−1622.

Tindle, A.G., and Breaks, F.W. (1998) Oxide minerals of the Separation Rapids rare-element granitic pegmatite group, northwestern Ontario. Canadian Mineralogist, 36, 609−635.

Wang, D., Mathur, R., Powell, W., Godfrey, L., and Zheng, Y.Y. (2019) Experimental evidence for fractionation of tin chlorides by redox and vapor mechanisms. Geochimica et Cosmochimica Acta, 250, 209−218.

Wang, F.X., Bagas, L., Jiang, S.H., and Liu, Y.F. (2017) Geological, geochemical, and geochronological characteristics of Weilasituo Sn-polymetal deposit, Inner Mongolia, China. Ore Geology Reviews, 80, 1206−1229.

Wang, J.B., Wang, Y.W., Wang, L.J., and Uemoto, T. (2001) Tin-polymetallic mineralization in the southern part of the Da Hinggan Mountains, China. Resource Geology, 51, 283−291.

Wang, T.H., She, J.X., Yin, K., Wang, K., Zhang, Y.J., Lu, X.C., Liu, X.D., and Li, W.Q. (2021) Sn (II) chloride speciation and equilibrium Sn isotope fractionation under hydrothermal conditions: a first principles study. Geochimica et Cosmochimica Acta, 300, 25−43.

Wang, X.Y., Fitoussi, C., Bourdon, B., and Amet, Q. (2017) A new method of Sn purification and isotopic determination with a double-spike technique for geological and cosmochemical samples. Journal of Analytical Atomic Spectromtry, 32, 1009−1019.

Wang, X.Y., Amet, Q., Fitoussi, C., and Bourdon, B. (2018) Tin isotope fractionation during magmatic processes and the isotope composition of the bulk silicate Earth. Geochimica et Cosmochimica Acta, 228, 320−335.

Wawryk, C.M., and Foden, J.D. (2015) Fe-isotope fractionation in magmatic-hydrothermal mineral deposits: A case study from the Renison Sn-W deposit, Tasmania. Geochimica et Cosmochimica Acta, 150, 285−298.

Weyer, S., and Ionov, D.A. (2007) Partial melting and melt percolation in the mantle: The message from Fe isotopes. Earth and Planetary Science Letters, 259, 119−133.

Wilkinson, J.J., Jenkin, G.R.T., Fallick, A.E., and Foster, R.P. (1995) Oxygen and hydrogen isotopic evolution of Variscan crustal fluids, south Cornwall, U.K. Chemical Geology, 123, 239−254.

Wilkinson, J.J., Weiss, D., Mason, T., and Coles, B. (2005) Zinc isotope variation in hydrothermal systems: preliminary evidence from the Irish Midlands ore field. Economic Geology, 100, 583−590.

Wille, G., Lerouge, C., and Schmidt, U. (2018) A multimodal micro-characterisation of trace element zonation and crystallographic orientation in natural cassiterite by combining cathodoluminescence, EBSD, EPMA and contribution of confocal Raman-in-SEM imaging. Journal of Microscopy, 270, 1−9.

Wilson, G.A., and Eugster, H. (1990) Cassiterite solubility and tin speciation in supercritical chloride solution. In: Spencer, R.J., Chou, I.M., (Eds.). Fluid-Mineral Interactions. A Tribute to H.P. Eugster, 2, Geochemical Society, Special Publication, pp. 179−195.

Wood, S.A., and Samson, I.M. (1998) Solubility of ore minerals and complexation of ore metals in hydrothermal solutions. Techniques in Hydrothermal Ore Deposits: In: Richards, J., Larson, P. (Eds.). Reviews in Economic Geology, 10, 33−80.

Yamazaki, E., Nakai, S., Yokoyama, T., Ishihara, S., and Tang, H.F. (2013) Tin isotope analysis of cassiterites from Southeastern and Eastern Asia. Geochemical Journal, 47, 21−35.

Yamazaki, E., Nakai, S., Sahoo, Y., Yokoyama, T., Mifune, H., Saito, T., Chen, J., Takagi, N., Hokanishi, N., and Yasuda, A. (2014) Feasibility studies of Sn isotope composition for provenancing ancient bronzes. Journal of Archaeological Science, 52, 458−467.

Yao, J.M., Mathur, R., Powell, W., Lehmann, B., Tornos, F., Wilson, M., and Ruiz, J. (2018) Sn-isotope fractionation as a record of hydrothermal redox reactions. American Mineralogist, 103, 1591−1598.

Yao, L., Lv, Z.C., Ye, T.Z., Pang, Z.S., Jia, H.X., Zhang, Z.H., Wu, Y.F., and Li, R.H. (2017) Zircon U-Pb ages, geochemical and Nd-Hf isotopic characteristics of quartz porphyry in the Baiyinchagan Sn polymetallic deposit, Inner Mongolia, southern Great Xing'an Range, China. Acta Petrologica Sinica, 33, 3183−3199 (in Chinese with English abstract).

Zhang, Y.S., Hou, T., Zhang, M.M., and Bian, X.F. (2018) Primary-regeneration hydrothermal fluid study—A case study of Dongshan mining district, Baiyinchagan, Inner Mongolia. Resource Information & Engineering, 33, 21−23 (in Chinese).

Zhou, J.B., Wilde, S.A., Zhang, X.Z., Zhao, G.C., Liu, F.L., Qiao, D.W., Ren, S.M., and Liu, J.H. (2011) A >1300 km late Pan-African metamorphic belt in NE China: New evidence from the Xing'an block and its tectonic implications. Tectonphysics, 509, 280−292.

This is the peer-reviewed, final accepted version for American Mineralogist, published by the Mineralogical Society of America.
The published version is subject to change. Cite as Authors (Year) Title. American Mineralogist, in press.
DOI: https://doi.org/10.2138/am-2022-8200. http://www.minsocam.org/

Figure captions

Fig. 1. (a) Schematic tectonic map of the northeast China; (b) Regional geological map of SGXR, showing the location of the tin deposits (modified after Mao et al., 2019); (c) Schematic diagram of the spatial distribution of main ore bodies in Weilasituo deposit; (d) Simplified geological map of the Baiyinchagan deposit (modified from Zhang et al., 2018); (e) Simplified geological map of the Maodeng deposit (modified from Liu, 1996).
(MOS: Mongolia-Okhotsk suture; EB: Erguna block; XB: Xing'an block; SLB: Songliao block; LXR-ZGCR: Lesser Xing'an Range-Zhangguangcai Range; JB: Jiamusi block; NCC: North China Craton)

Fig. 2. Diagrams for Fe_2O_3 *vs.* SiO_2 (a), Nb/Ta *vs.* TE_{1-3} (Irber, 1999) (b), Nb/Ta *vs.* Zr/Hf (c) and K/Rb *vs.* Rb (d), showing the geochemical characteristics of the ore-related granitic rocks.
Data resource: Weilasituo, after Gao et al. (2019) and Wang et al. (2017); Baiyinchagan, after Yao et al. (2017) and Liu et al. (2017); Maodeng, after Guo et al. (2019).

Fig. 3. CL images and trace element contents (in ppm) of cassiterite from the Weilasituo (a-d), Baiyinchagan (e) and Maodeng (f) deposits. Red circles are the laser ablation spots for trace elements with the size of 50 μm in diameter.

Fig. 4. LA-ICPMS multiple element mapping results of representative cassiterite grain (NW-N-72) from Weilasituo sample. The CL image of this grain is shown in Fig. 3D.

Fig. 5. LA-ICPMS multiple element mapping results of representative cassiterite grain (WM-7) from Maodeng sample. The CL image of this grain is shown in Fig. 3F.

Fig. 6. Binary plots of selected trace elements in cassiterite from the NE China.

Fig. 7. Tin isotope compositions of all cassiterite grains, analysed in this study, show plot on

a mass-dependent fractionation line in the $\delta^{124}/^{117}$Sn *vs.* $\delta^{122}/^{118}$Sn space. All delta values are given with twofold standard error 2 SE. Data from Cornwall, Indonesia and Bolivia of Schulze et al. (2017) are included in Fig. 7d for comparison.

Fig. 8. Rayleigh distillation model predicting the range of $\delta^{124}/^{117}$Sn in the fluid that would evolve, assuming progressive precipitation from an evolving solution. F is the proportion of Sn in the magma relative to that in the fluid. The starting $\delta^{124}/^{117}$Sn values of the GSP-2 is 0.61 ‰ relative to the Sn NIST SRM 3161a standard solution (Creech et al., 2017; She et al., 2020). The curves for a range of different α-fractionation factors for cassiterite (α=0.983, from Creech et al. (2019b); α=0.99897, from She et al. (2020)) and pairs cassiterite-stannite (calculated based on the data from Yao et al. (2018)) are shown.

Fig. 9. Diagram for $\delta^{124}/^{117}$Sn *vs.* Ti/Zr ratios, showing a general shift towards light Sn isotope compositions in cassiterite correlated with decreasing Ti/Zr ratios.

Fig. 10. Plot of fraction of precipitated Sn and the evolving Sn isotopic composition of the precipitated Sn in a transport-precipitation model (after Wang et al., 2021), by assuming dominance of different Sn species in the hydrothermal fluid.
For a detail explanation of the model, see Wang et al. (2021). The temperatures used here are the average values of the peak homogenization temperature of different stages from the fluid studies of Liu et al. (2018b), Liu et al. (1996), and the mineralization temperature calculated from the co-existing sphalerite thermometer (Liu et al., 2017).
Numbers in plot refer to: 1-Weilasituo deposit; 2-Baiyinchagan deposit; 3- Maodeng deposit.

Fig. 11. Complementary dataset comprising reliable Sn isotopes of tin ores. The shaded box represents the bulk silicate Earth (BSE) composition of Wang et al. (2018). Data sources: Precambrian cassiterite, after Brügmann et al. (2017); late Paleozoic cassiterite, after Yao et al. (2018) and Haustein et al. (2010); early Mesozoic cassiterite, after Wang et al. (2019); late Mesozoic cassiterite, after this study; Cenozoic cassiterite, after Yao et al. (2018); Cassiterite as placer-tin, after Haustein et al. (2010); stannites from Yao et al. (2018), Haustein et al.

(2010) and Brügmann et al. (2017).

Table captions

Table 1 Description of cassiterite samples analyzed in this study.

Table 2 Sn stable isotope and concentration results (mean values) for cassiterites by UV-*fs* LA-MC-ICPMS.

Table 1 Location and description of the cassiterite samples.

Sample	Sample location	Mineral assemblages	Description	Mineraliation stage
Weilasituo Sn-W-Li polymetallic deposit				
NW-N-30, 19G2NW-30	Level 2 of the South inclined well; Wellhead: E 117°27′59″, N 44°5′32″	Qtz+Sp+Cst	Quartz-vein ores with euhedral coarse cassiterite surrounded by disseminated sphalerite. Cassiterite as 1-2 cm large crystals.	Early stage (high–temperature hydrothermal stage)
NW-N-28	Level 2 of the South inclined well; Wellhead: E 117°27′59″, N 44°5′32″	Qtz+Znw+Sp+Cst	Subhedral fine grain cassiterite in massive quartz, with sphalerite is locally developed.	Early stage
NW-N-31, NW19G02	Level 2 of the South inclined well; Wellhead: E 117°27′59″, N 44°5′32″	Qtz+Sp+Cst	Quartz-vein ores with euhedral coarse cassiterite surrounded by disseminated sphalerite. Cassiterite as ~1 cm large crystals.	Early stage
NW-X-72	E 117°28′43″, N 44°5′13″	Qtz+Cc+Mo+Sp+Cst+Py	Molybdenite and cassiterite coexist in massive quartz and calcite. Pyrite is continuously fine-grained distributed.	Early stage
NW-N-101	Level 2 of the South inclined well; Wellhead: E 117°27′59″, N 44°5′32″	Qtz+Fl+Cst+Wf	Cassiterite and wolframite bearing quartz-flurite geode.	Late stage (late hydrothermal stage)
WL-04, 1807WL4a	Level 2 of the North inclined well; Wellhead: E 117°27′56″, N 44°5′18″	Qtz+Cc+Znw+Cst	Cassiterite bearing quartz-zinnwaldite vein cross-cutting biotite plagioclase gneiss of the Xilinguole Formation.	Late stage
Baiyinchagan Sn-Ag-Pb-Zn deposit				
BY1908, 18BY0709a	E 117°10′15″, N 43°52′05″	Qtz+Sp+Ccp+Py+Ga+Apy+Cst	Massive polymetallic sulphides in quartz-chlorite lode cross cutting tuffaceous sandstone of the Dashizhai Formation.	Early stage (cassiterite-sulfide stage)

BY1909, 18BY0715	E 117°10′36″, N 43°52′18″	Qtz+Py+Ccp+Cst	Polymetallic sulphide lode with quartz cross cuttin sandstone of the Dashizhai Formation. Cassiterite is fine-grained and as <1 mm crystals.	Early stage
BY1910, 18BY0716	E 117°11′08″, N 43°51′46″	Qtz+Py+Cst	Cassiterite and pyrite bearing quartz geode.	Late stage (low temperature hydrothermal stage)
Maodeng Sn-Cu deposit				
WM-4	E 116°32′40″, N 44°11′38″	Qtz+Ccp+Apy+Cst±Py	Coarse cassiterite-chalcopyrite bearing quartz vein cross-cutting carbonaceous slate sandstone.	Early stage (quartz-cassiterite-wolframite)
WM-5, 18WM0802	E 116°32′25″, N 44°11′13″	Qtz+Cst+Apy+Py	Coarse cassiterite bearing quartz vein cross-cutting carbonaceous slate sandstone.	Early stage
WM-7, 18WM0804X	E 116°31′03″, N 44°10′20″	Qtz+Cst+Po+Py	Euhedral coarse cassiterite surrounded by pyrrhotite and pyrite.	Late stage (late veinlets)
MD1901, MD-1902, MD-1903	E 116°31′37″, N 44°10′52″	Qtz+Cst	Cassiterite bearing quartz vein cross-cutting slate.	Late stage

Notes: Qtz, quartz; Cc, calcite; Znw, zinnwaldite; Fl, fluorite; Sp, sphalerite; Cst, cassiterite; Ccp, chalcopyrite; Py, pyrite; Apy, asenopyrite; Ga, galena; Po, pyrrhotite; Wf, wolframite.

Table 2 Sn stable isotope and concentration results (mean values) for cassiterites by UV-*fs* LA-MC-ICPMS.

Sample	Stage	$^{122}/^{118}$Sn	2SE	$^{124}/^{117}$Sn	2SE	n
In-house standard	/	0.00	0.01	0.01	0.02	369
Weilasituo deposit						
NW-N-30	Early	-0.03	0.03	-0.03	0.04	9
19G2NW-30	Early	-0.23	0.03	-0.23	0.03	5
NW-N-28	Early	-0.22	0.03	-0.33	0.04	5
NW-N-31	Early	-0.13	0.03	-0.19	0.04	7
NW19G02	Early	-0.12	0.03	-0.18	0.04	9
NW-N-72	Early	0.03	0.04	0.06	0.04	9
NW-N-101	Late	-0.06	0.04	-0.11	0.04	4
WLST-04	Late	0.32	0.03	0.59	0.03	20
1807WL4a	Late	-0.46	0.04	-0.66	0.05	10
Baiyinchagan deposit						
BY1908	Early	-0.39	0.02	-0.64	0.04	12
18BY0709a	Early	-0.29	0.03	-0.50	0.04	8
BY1909	Early	-0.53	0.03	-0.86	0.04	13
18BY0715	Early	-0.71	0.04	-1.25	0.06	6
BY1910	Late	-0.35	0.02	-0.52	0.03	17
18BY0716	Late	-0.85	0.04	-1.43	0.06	7
Maodeng deposit						
WM-4	Early	0.32	0.07	0.62	0.08	3
WM-5	Early	0.01	0.05	0.16	0.05	6
18WM0802	Early	0.30	0.04	0.59	0.04	9
WM-7	Late	0.13	0.03	0.28	0.04	10
18WM0804X	Late	0.03	0.03	0.11	0.04	10
MD-1901	Late	0.26	0.03	0.54	0.04	10
MD-1902	Late	0.16	0.03	0.31	0.05	9
MD-1903	Late	0.03	0.04	0.12	0.06	6

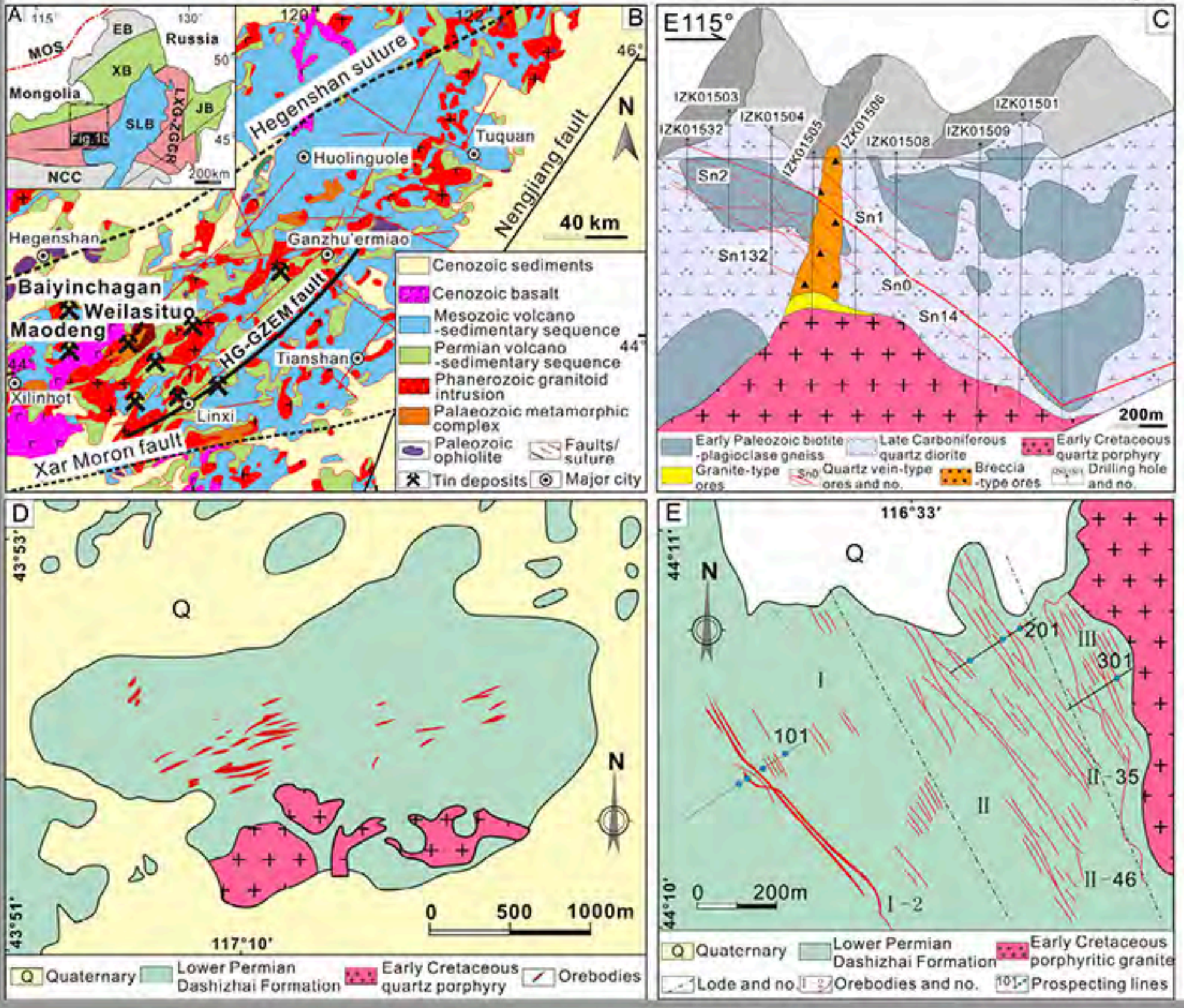
A
115°
130°
EB
Russia
MOS
50°
XB
Mongolia
JB
SLB
LXQ-CGCR
Fig. 1b
45°
NCC
200km
B
120°
Hegenshan suture
Huolinguole
Tuquan
Nengjiang fault
N
46°
40 km
Hegenshan
Ganzhu'ermiao
Baiyinchagan
Weilasituo
Maodeng
HG-GZEM fault
Tianshan
44°
Xilinhot
Linxi
Xar Moron fault
Cenozoic sediments
Cenozoic basalt
Mesozoic volcano -sedimentary sequence
Permian volcano -sedimentary sequence
Phanerozoic granitoid intrusion
Palaeozoic metamorphic complex
Paleozoic ophiolite
Faults/ suture
Tin deposits
Major city
C
E115°
IZK01503
IZK01504
IZK01532
IZK01505
IZK01506
IZK01508
IZK01501
IZK01509
Sn2
Sn1
Sn132
Sn0
Sn14
200m
Early Paleozoic biotite -plagioclase gneiss
Late Carboniferous quartz diorite
Early Cretaceous quartz porphyry
Granite-type ores
Sn0 Quartz vein-type ores and no.
Breccia -type ores
Drilling hole and no.
D
43°53'
Q
N
0
500
1000m
43°51'
117°10'
Quaternary
Lower Permian Dashizhai Formation
Early Cretaceous quartz porphyry
Orebodies
E
116°33'
44°11'
Q
N
201
III
301
I
101
II-35
II
II-46
0
200m
I-2
44°10'
Quaternary
Lower Permian Dashizhai Formation
Early Cretaceous porphyritic granite
Lode and no.
I-2 Orebodies and no.
101 Prospecting lines

Fig. 2

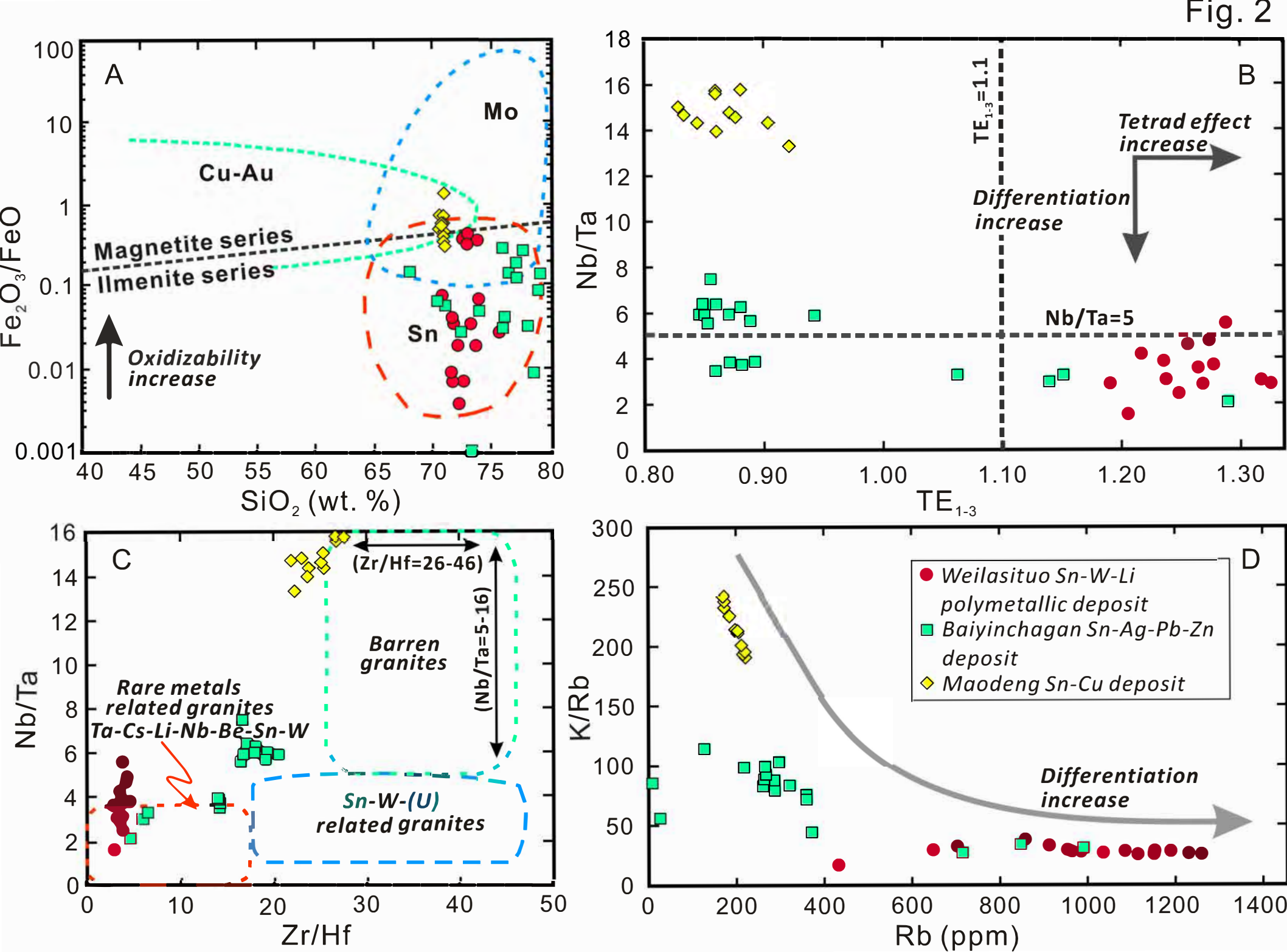
A
Mo
Cu-Au
Magnetite series
Ilmenite series
Sn
Oxidizability increase
Fe2O3/FeO
SiO2 (wt. %)
B
TE1-3=1.1
Tetrad effect increase
Differentiation increase
Nb/Ta=5
Nb/Ta
TE1-3
C
(Zr/Hf=26-46)
(Nb/Ta=5-16)
Barren granites
Rare metals related granites Ta-Cs-Li-Nb-Be-Sn-W
Sn-W-(U) related granites
Nb/Ta
Zr/Hf
D
Weilasituo Sn-W-Li polymetallic deposit
Baiyinchagan Sn-Ag-Pb-Zn deposit
Maodeng Sn-Cu deposit
Differentiation increase
K/Rb
Rb (ppm)

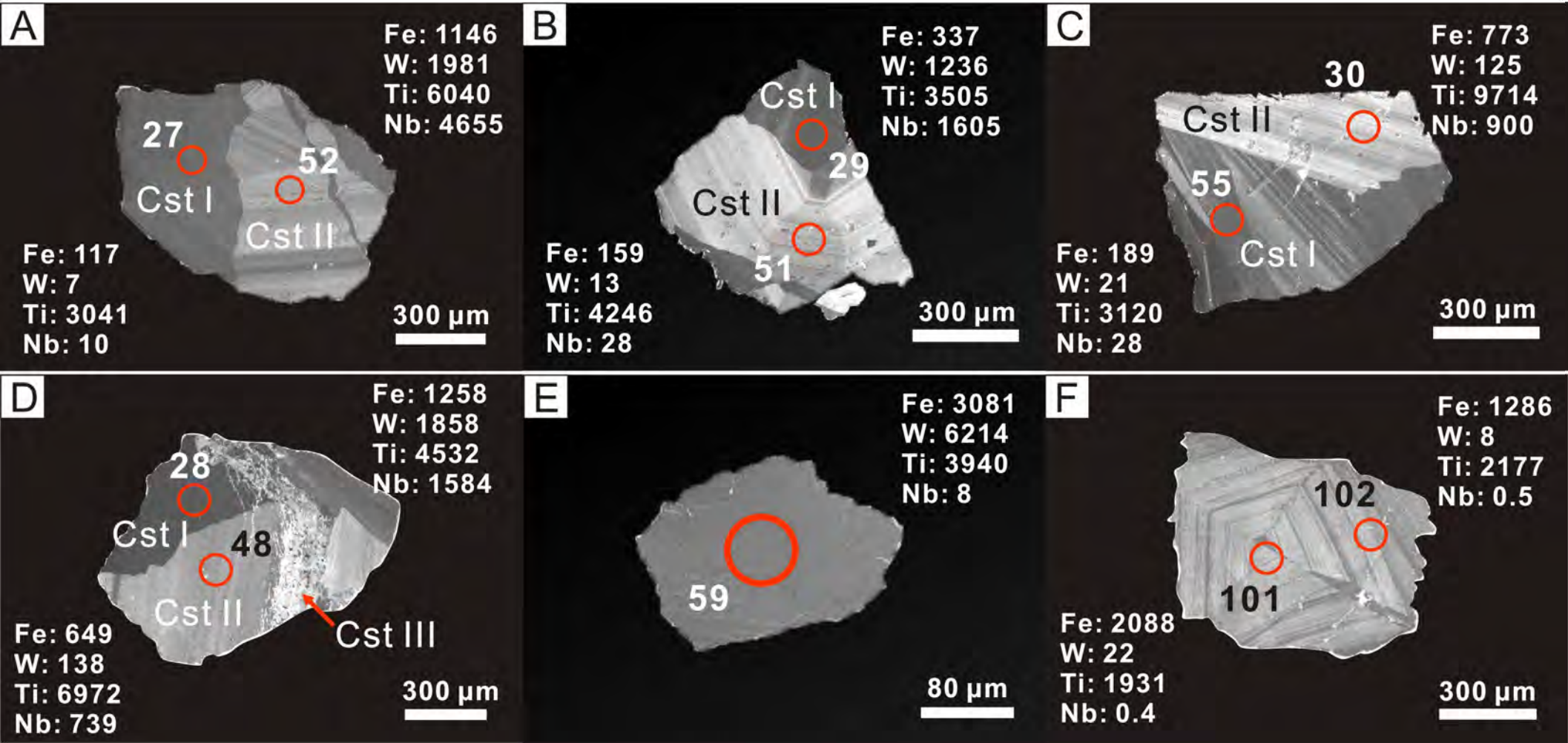
A
Fe: 1146
W: 1981
Ti: 6040
Nb: 4655
27
52
Cst I
Cst II
Fe: 117
W: 7
Ti: 3041
Nb: 10
300 μm
B
Fe: 337
W: 1236
Ti: 3505
Nb: 1605
Cst I
29
Cst II
51
Fe: 159
W: 13
Ti: 4246
Nb: 28
300 μm
C
Fe: 773
W: 125
Ti: 9714
Nb: 900
30
Cst II
55
Cst I
Fe: 189
W: 21
Ti: 3120
Nb: 28
300 μm
D
Fe: 1258
W: 1858
Ti: 4532
Nb: 1584
28
Cst I
48
Cst II
Cst III
Fe: 649
W: 138
Ti: 6972
Nb: 739
300 μm
E
Fe: 3081
W: 6214
Ti: 3940
Nb: 8
59
80 μm
F
Fe: 1286
W: 8
Ti: 2177
Nb: 0.5
102
101
Fe: 2088
W: 22
Ti: 1931
Nb: 0.4
300 μm

Fig. 4

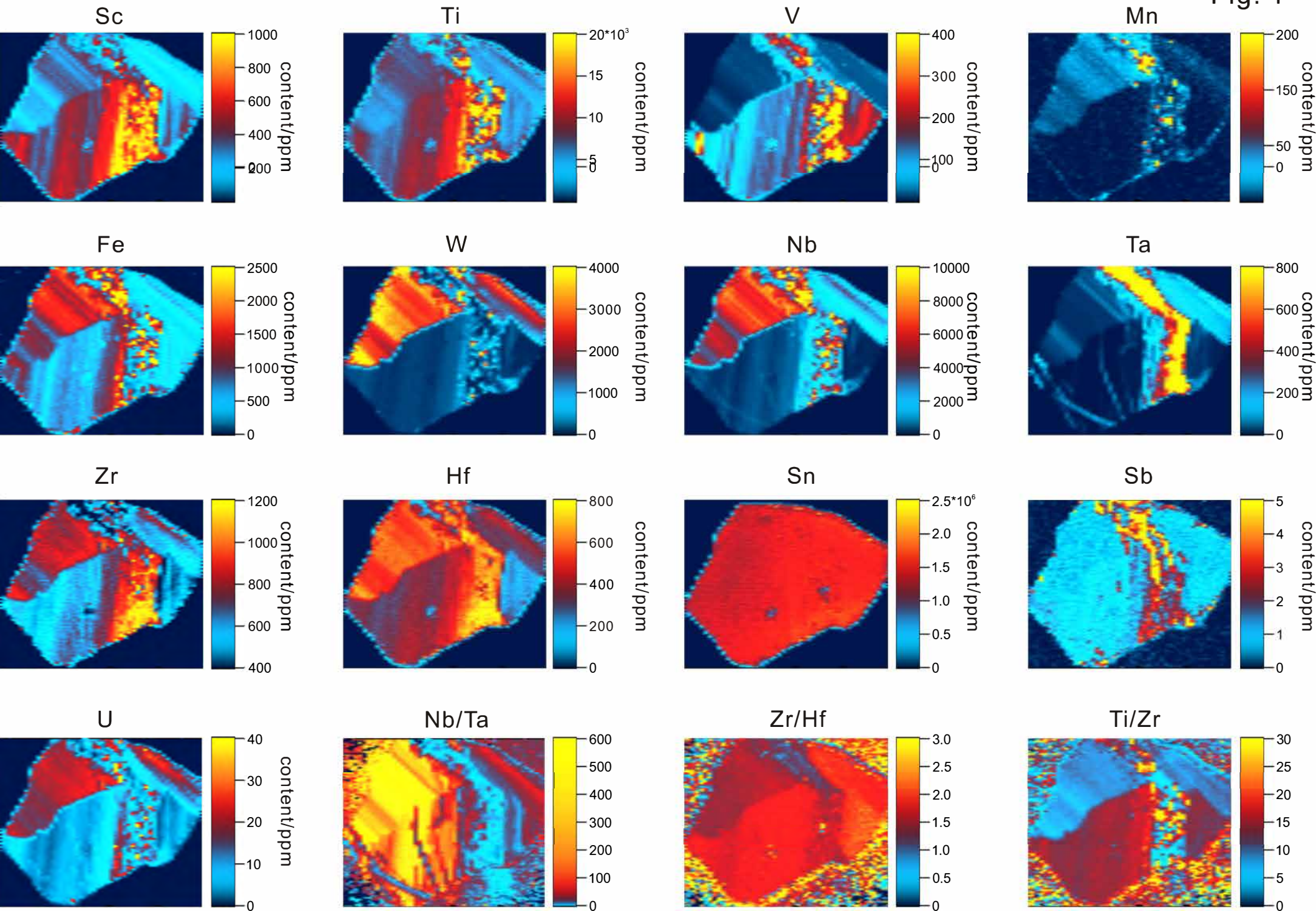
Sc
1000
800
600
400
200
content/ppm
Ti
20*10³
15
10
5
0
content/ppm
V
400
300
200
100
0
content/ppm
Mn
200
150
50
0
content/ppm
Fe
2500
2000
1500
1000
500
0
content/ppm
W
4000
3000
2000
1000
0
content/ppm
Nb
10000
8000
6000
4000
2000
0
content/ppm
Ta
800
600
400
200
0
content/ppm
Zr
1200
1000
800
600
400
content/ppm
Hf
800
600
400
200
0
content/ppm
Sn
2.5*10⁶
2.0
1.5
1.0
0.5
0
content/ppm
Sb
5
4
3
2
1
0
content/ppm
U
40
30
20
10
0
content/ppm
Nb/Ta
600
500
400
300
200
100
0
Zr/Hf
3.0
2.5
2.0
1.5
1.0
0.5
0
Ti/Zr
30
25
20
15
10
5
0

Fig. 5

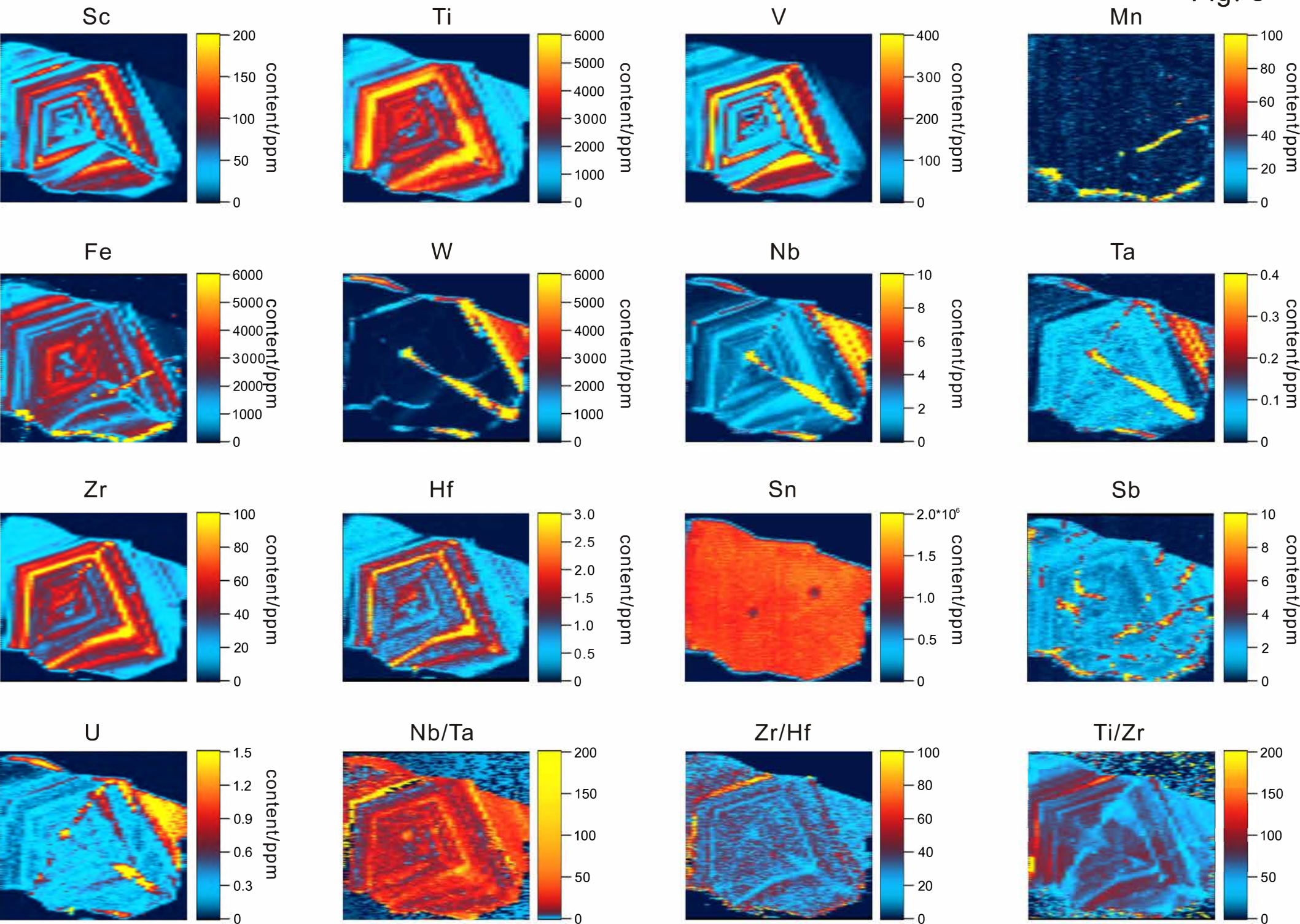
Sc
200
150
100
50
0
content/ppm
Ti
6000
5000
4000
3000
2000
1000
0
content/ppm
V
400
300
200
100
0
content/ppm
Mn
100
80
60
40
20
0
content/ppm
Fe
6000
5000
4000
3000
2000
1000
0
content/ppm
W
6000
5000
4000
3000
2000
1000
0
content/ppm
Nb
10
8
6
4
2
0
content/ppm
Ta
0.4
0.3
0.2
0.1
0
content/ppm
Zr
100
80
60
40
20
0
content/ppm
Hf
3.0
2.5
2.0
1.5
1.0
0.5
0
content/ppm
Sn
2.0*10^6
1.5
1.0
0.5
0
content/ppm
Sb
10
8
6
4
2
0
content/ppm
U
1.5
1.2
0.9
0.6
0.3
0
content/ppm
Nb/Ta
200
150
100
50
0
Zr/Hf
100
80
60
40
20
0
Ti/Zr
200
150
100
50
0

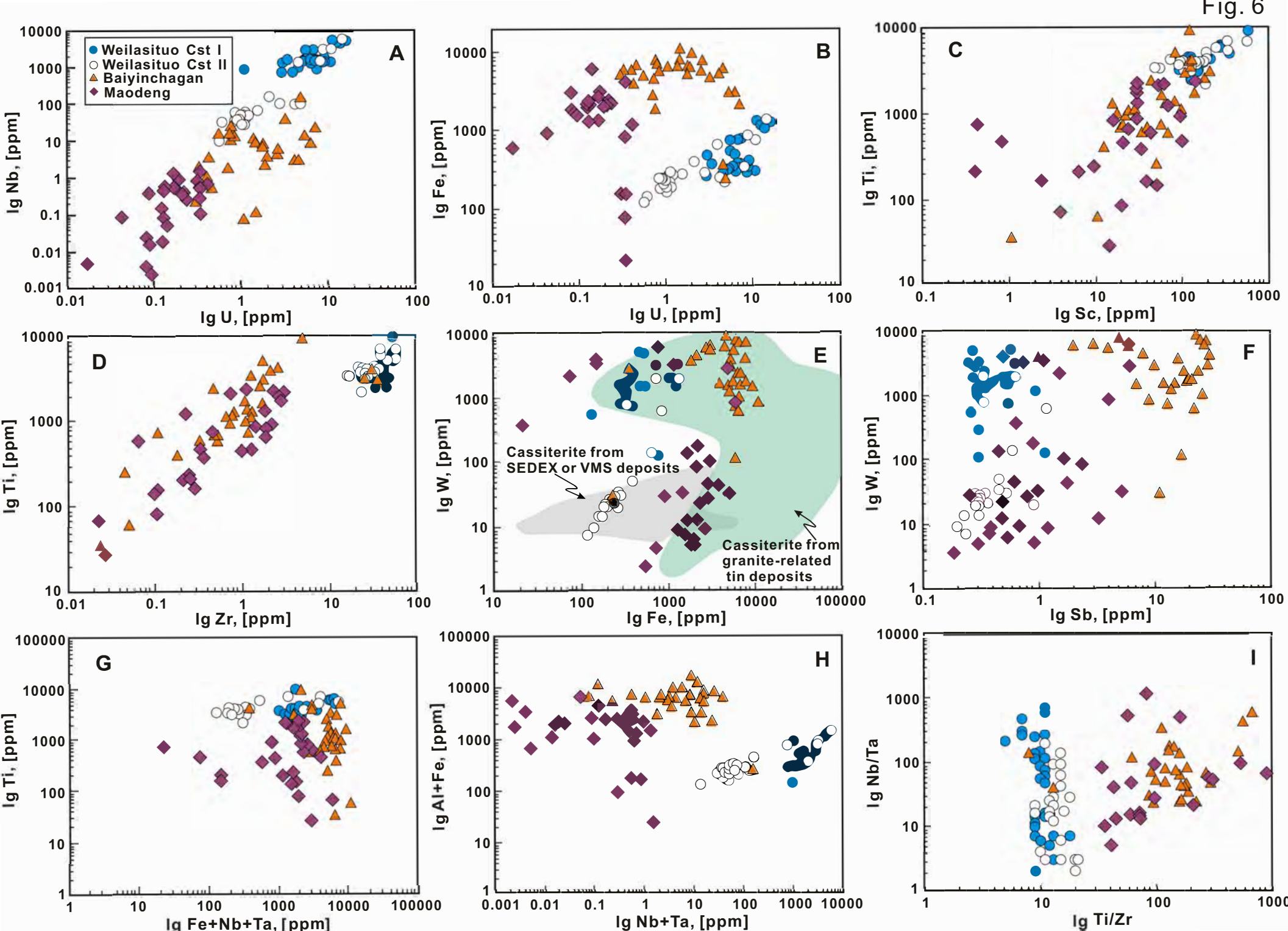
Weilasituo Cst I
Weilasituo Cst II
Baiyinchagan
Maodeng
A
lg Nb, [ppm]
lg U, [ppm]
B
lg Fe, [ppm]
lg U, [ppm]
C
lg Ti, [ppm]
lg Sc, [ppm]
D
lg Ti, [ppm]
lg Zr, [ppm]
E
lg W, [ppm]
lg Fe, [ppm]
Cassiterite from SEDEX or VMS deposits
Cassiterite from granite-related tin deposits
F
lg W, [ppm]
lg Sb, [ppm]
G
lg Ti, [ppm]
lg Fe+Nb+Ta, [ppm]
H
lg Al+Fe, [ppm]
lg Nb+Ta, [ppm]
I
lg Nb/Ta
lg Ti/Zr

Fig. 7

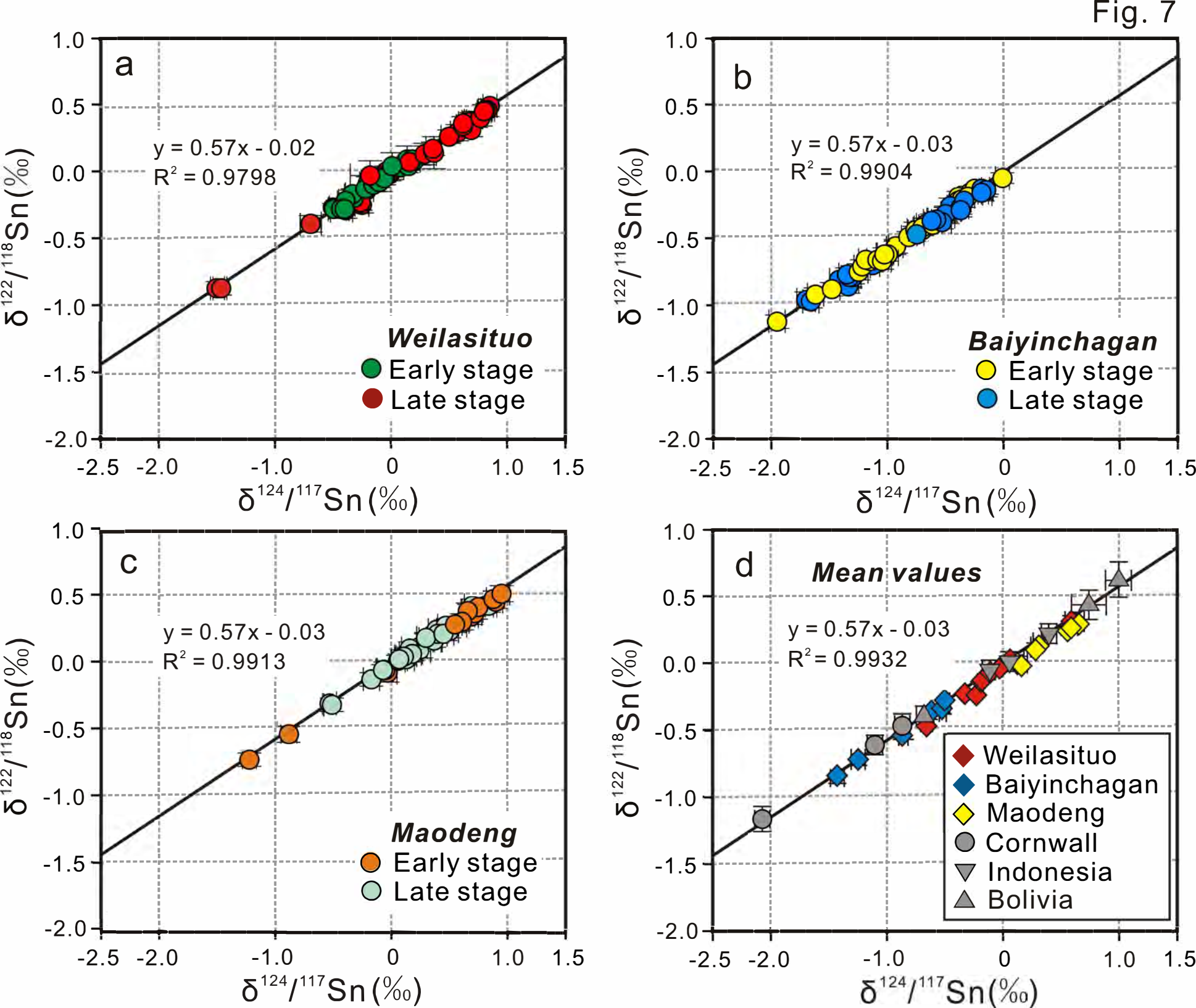
a
y = 0.57x - 0.02
R² = 0.9798
Weilasituo
Early stage
Late stage
b
y = 0.57x - 0.03
R² = 0.9904
Baiyinchagan
Early stage
Late stage
c
y = 0.57x - 0.03
R² = 0.9913
Maodeng
Early stage
Late stage
d
Mean values
y = 0.57x - 0.03
R² = 0.9932
Weilasituo
Baiyinchagan
Maodeng
Cornwall
Indonesia
Bolivia
δ122/118Sn (‰)
δ124/117Sn (‰)

Fig. 8

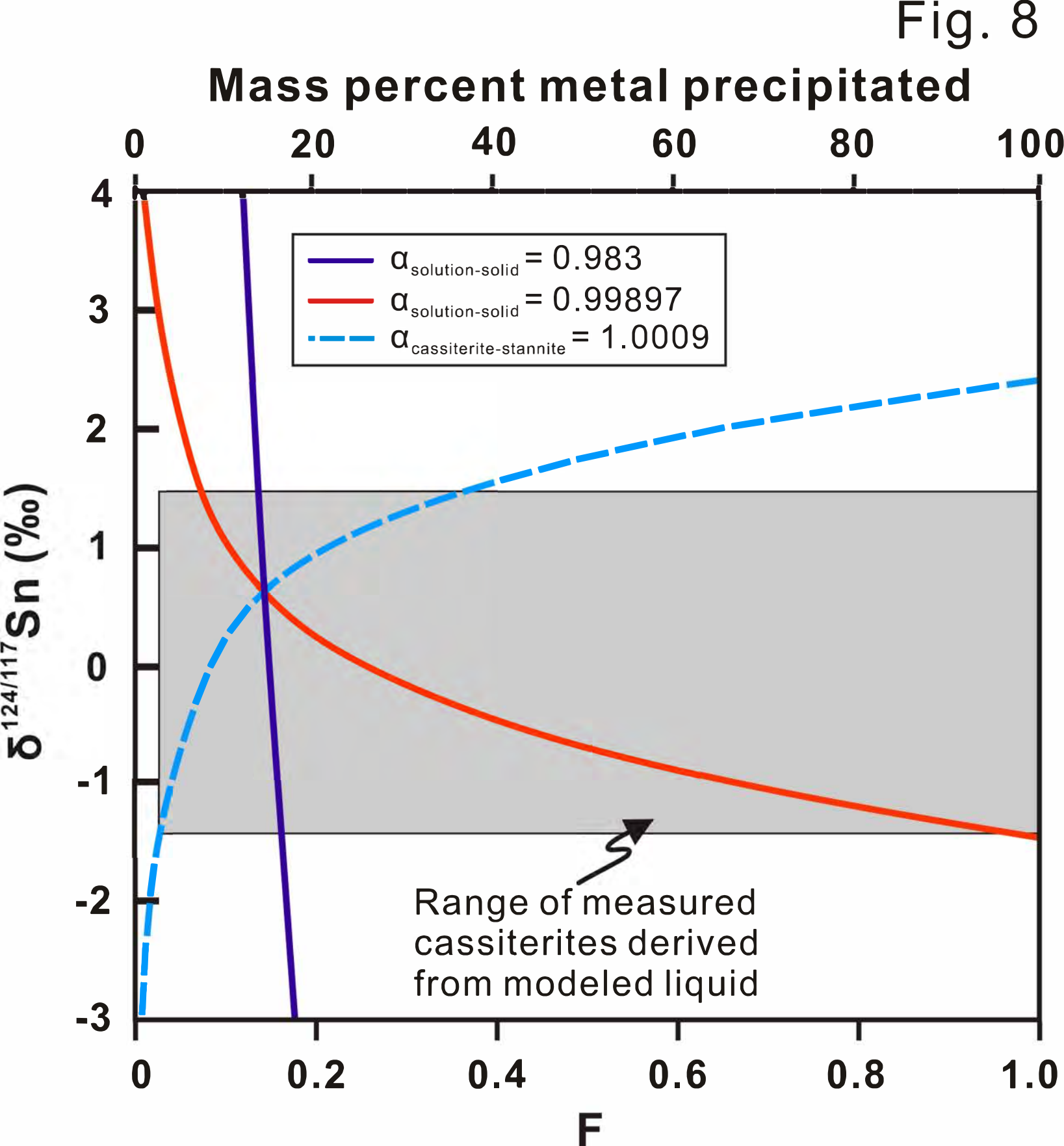
Mass percent metal precipitated
0
20
40
60
80
100
4
3
2
1
0
-1
-2
-3
$\delta^{124/117}$Sn (‰)
$\alpha_{solution\text{-}solid}$ = 0.983
$\alpha_{solution\text{-}solid}$ = 0.99897
$\alpha_{cassiterite\text{-}stannite}$ = 1.0009
Range of measured cassiterites derived from modeled liquid
0
0.2
0.4
0.6
0.8
1.0
F

Fig. 9

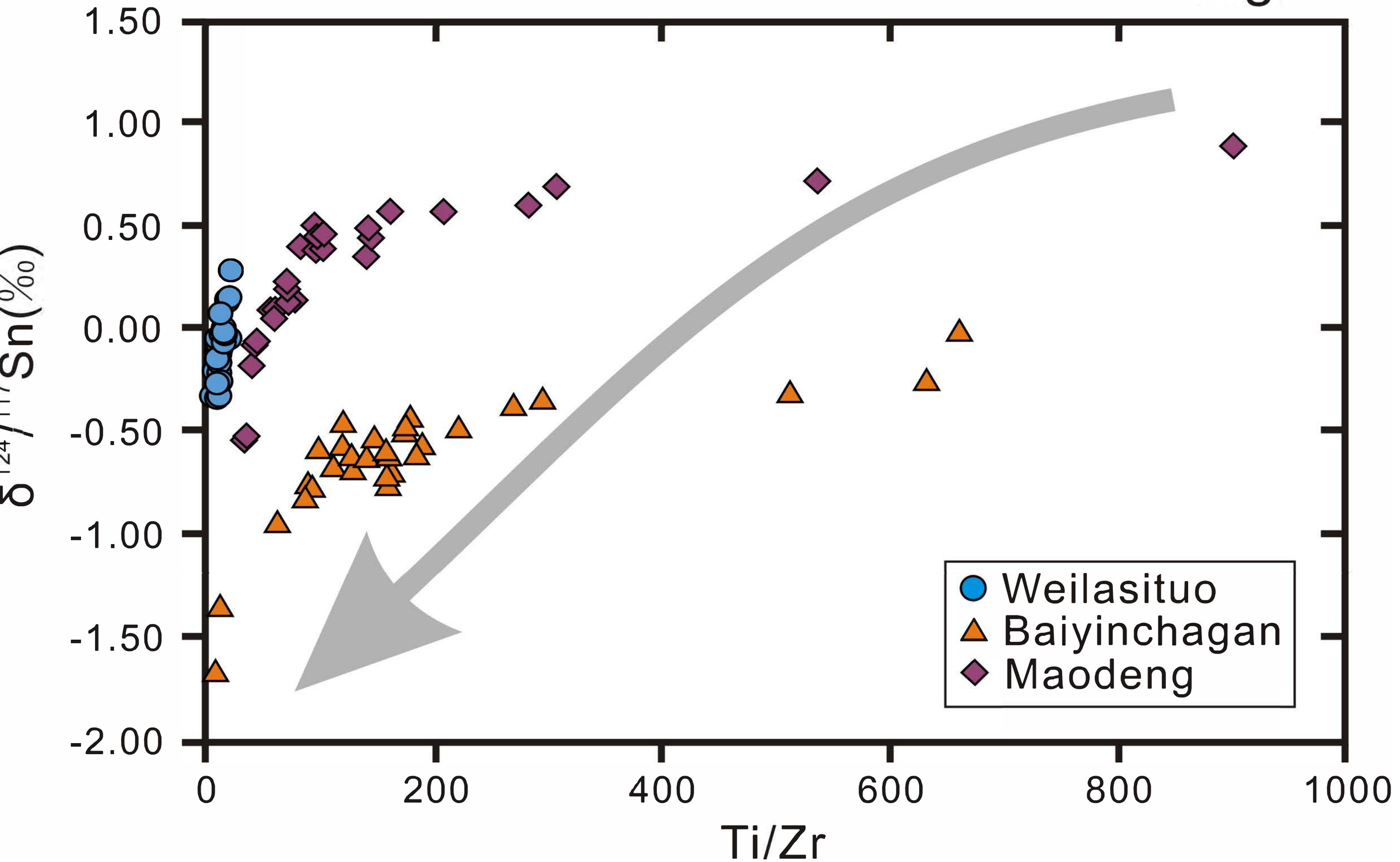
1.50
1.00
0.50
0.00
-0.50
-1.00
-1.50
-2.00
δ124/117Sn(‰)
0
200
400
600
800
1000
Ti/Zr
Weilasituo
Baiyinchagan
Maodeng

Fig. 10

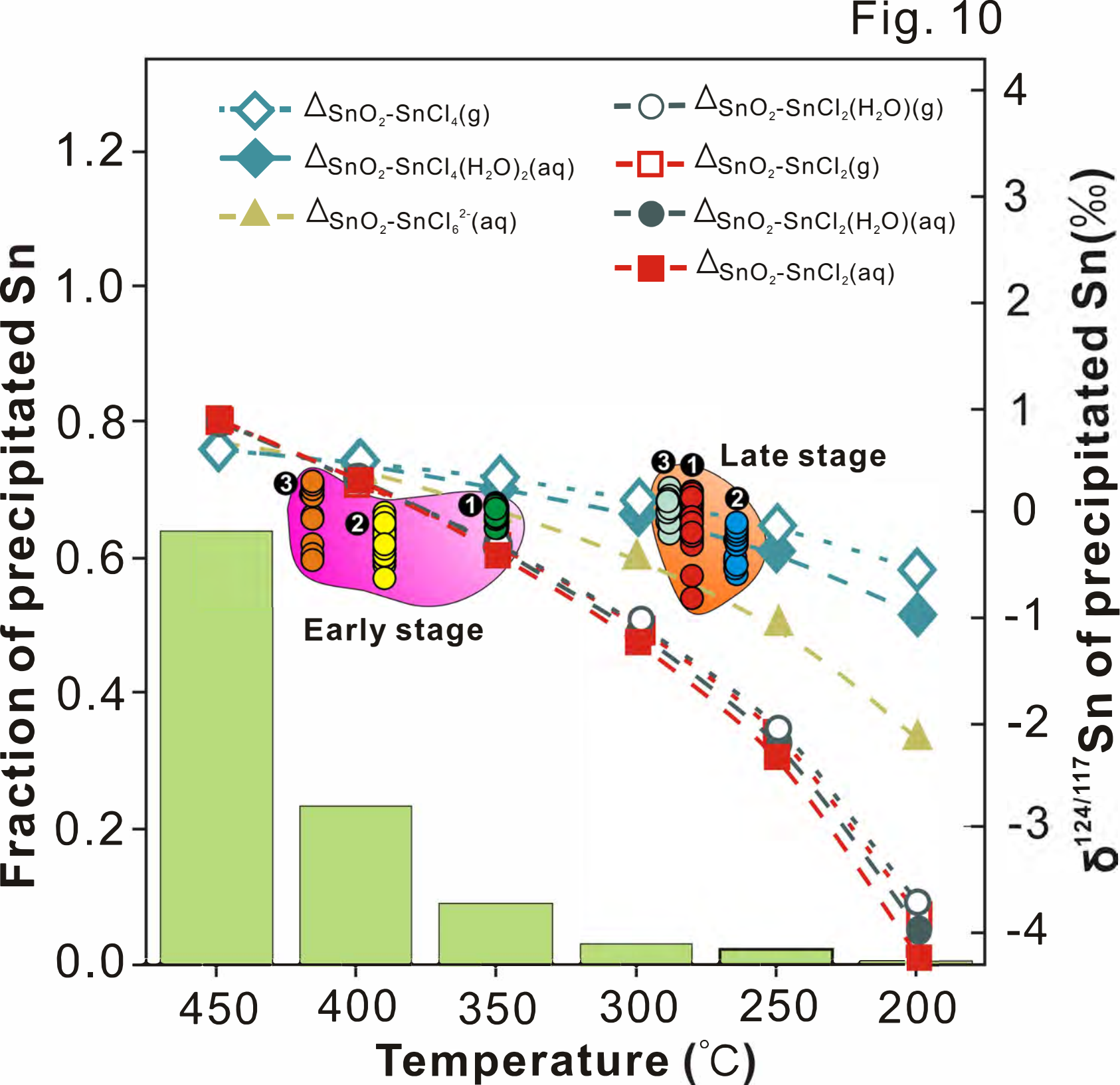
$\Delta_{SnO_2\text{-}SnCl_4(g)}$
$\Delta_{SnO_2\text{-}SnCl_4(H_2O)_2(aq)}$
$\Delta_{SnO_2\text{-}SnCl_6^{2-}(aq)}$
$\Delta_{SnO_2\text{-}SnCl_2(H_2O)(g)}$
$\Delta_{SnO_2\text{-}SnCl_2(g)}$
$\Delta_{SnO_2\text{-}SnCl_2(H_2O)(aq)}$
$\Delta_{SnO_2\text{-}SnCl_2(aq)}$
Early stage
Late stage
Fraction of precipitated Sn
$\delta^{124/117}$Sn of precipitated Sn(‰)
Temperature (℃)
1.2
1.0
0.8
0.6
0.4
0.2
0.0
4
3
2
1
0
-1
-2
-3
-4
450
400
350
300
250
200

Fig. 11

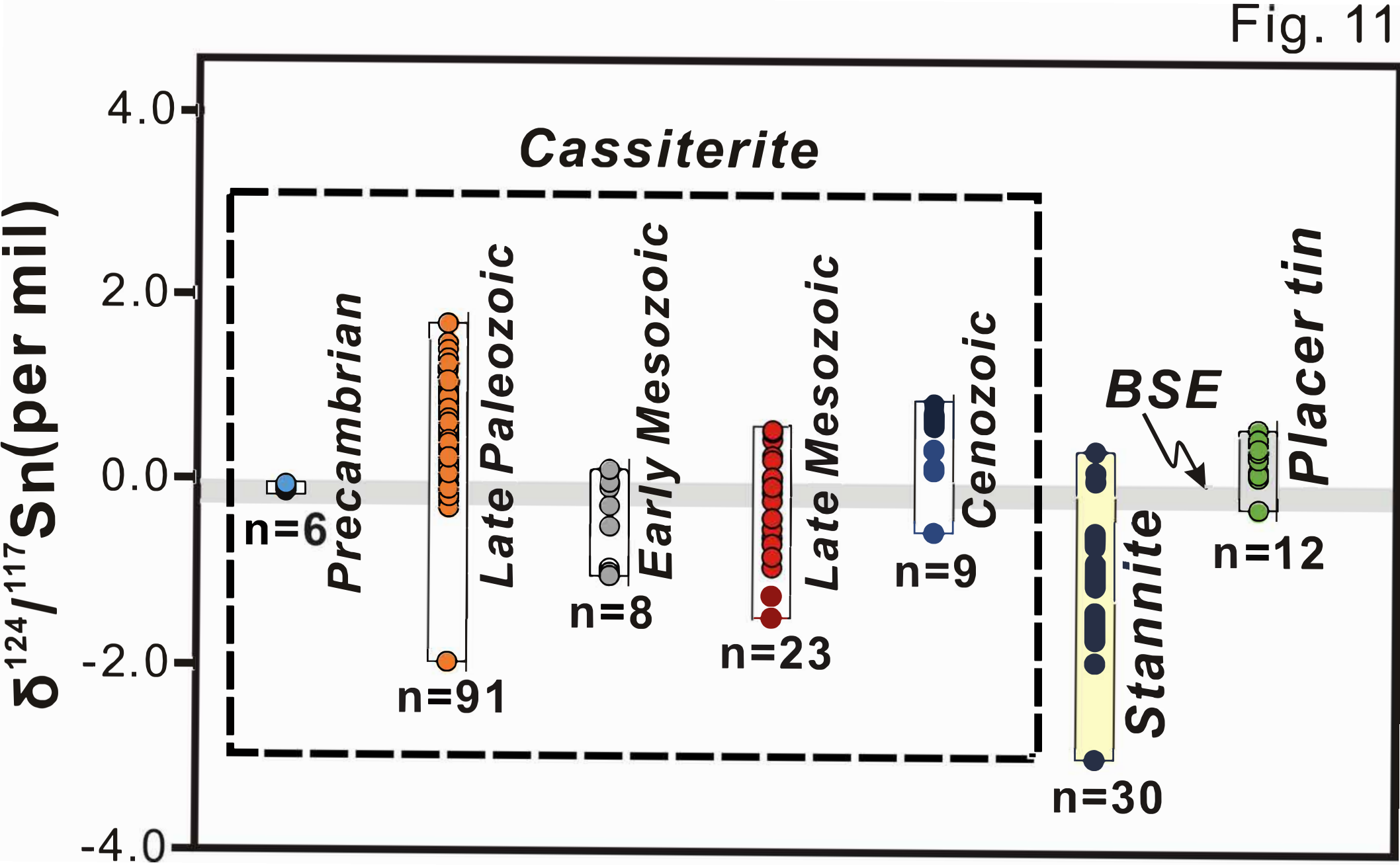
Cassiterite
δ124/117Sn(per mil)
4.0
2.0
0.0
-2.0
-4.0
n=6
Precambrian
n=91
Late Paleozoic
n=8
Early Mesozoic
n=23
Late Mesozoic
n=9
Cenozoic
BSE
n=30
Stannite
n=12
Placer tin